Title

The effects of nearby fractures on hydraulically induced fracture propagation and permeability changes

Authors

Figueiredo, Bruno
Tsang, Chin-Fu
Rutqvist, Jonny
et al.

Publication Date

2017-10-01

DOI

10.1016/j.enggeo.2017.08.011

Peer reviewed

The effects of nearby fractures on hydraulically induced fracture propagation and permeability changes

Bruno Figueiredo, Chin-Fu Tsang, Jonny Rutqvist, Auli Niemi

Abstract

Fracture propagation caused by hydraulic fracturing operations can be significantly influenced by adjacent fractures. This paper presents a detailed coupled hydro-mechanical analysis to study the effects of nearby natural fractures on hydraulically induced fracture propagation and changes in fracture permeability. Two rock domains were considered in comparison: FD1, with one fracture, and FD2, with two adjacent parallel or non-parallel fractures. It was assumed that water injection occurred in a borehole that intersected the single fracture in FD1 and one of the two fractures in FD2. Simulations were made for a time period of 3 h with an injection period of 2 h followed by 1 h of shut-in. An elastic-brittle model based on the degradation of material properties was implemented in a 2D finite-difference scheme and used for elements of the intact rock subjected to tension and shear failure. The intact rock was considered to have a low but non-negligible permeability. A verification study against analytical solutions showed that the fracture propagation and stress concentrationsdue to differential boundary stresses could be accurately represented by our model. Next, a base case was considered, in which the stress ratio (SR) between the magnitudes of the maximum and minimum boundary stresses, the permeability k_R of the intact rock and the initial permeability k_{TF} of the tension failure regions were fixed. In FD2, the distance $d_F$between the two natural fractures defined by the closest distance was also fixed. The results showed that in both rock domains, the fracture started to propagate when the pore pressurewas approximately 85% of the magnitude of the minimum boundary stress. The propagation of a single fracture was significantly greater than the propagation of a double fracture system because, in the latter case, the pore pressure decreased when the two fractures connected. As a result, changes in permeability in FD2 were smaller than in FD1. At the end of injection, the maximum ratios between the final and initial permeability of the natural fractures were found to be approximately 3 and 2 for rock domains FD1 and FD2, respectively. For non-parallel fractures, the controlling factor for fracture propagation was the separation between the tips of the pressurised fracture and the neighbouring non-pressurised fracture. A sensitivity study was conducted to study the influence of the key parameters d_F, SR, k_R and k_{TF} on the simulation results. Fracture propagation showed more sensitivity to d_F and SRthan to the other parameters.

Keywords: Hydraulic fracturing stimulation, Coupled hydro-mechanical effects, Fracture propagation and connectivity, Permeability changes, Elastic-brittle model

1. Introduction

Hydraulic fracturing is a method used routinely in oil and gas exploitation and in enhanced geothermal systems. This method is a technique that creates fractures in deep rock formations by high-pressure fluid injection and thus increases flow permeability in the injection region. Hydraulic fracturing stimulation leads to changes in pore pressure and effective normal stress across the created fractures, which in turn leads to consequential fracture propagation. Hence, the fracture permeability depends on the *in situ* stress conditions and on the pressure of the flowing fluid (Min et al., 2004). Hydro-mechanical coupling is an important issue that must be taken into account (Rutqvist and Stephansson, 2013, Tsang and Niemi, 2013).

To understand the fracturing processes, several laboratory experiments and 2D and 3D numerical studies have been performed by many researchers. In these studies, the fracture closure, extension and mechanical interactions for parallel and quasi-parallel fractures have been analysed (Germanovich & Askakhov, 2004). Laboratory experiments were conducted in gypsum and marble (Bobet and Einstein, 1998, Wong and Einstein, 2009a, Wong and Einstein, 2009b) to understand the fracture propagation caused by differential boundary stresses. In (Morgan et al., 2013), samples of granite with single and double flaw geometries under quasi-static vertical compressive loads were tested. In (Zang et al., 1998), fractures were created by compressing granite cores uniaxially. In (Mayer et al., 2011), fracture propagation in sandstones induced by increases in the confining stresses and pore pressure was studied.

Numerical continuum- and discrete-based models have been applied to study fracture propagation induced by hydraulic injection pressure under confining stresses. Continuum-based models have used the finite element method (Moes and Belytschko, 1999, Gonçalves da Silva and Einstein, 2013, Nguyen et al., 2017, Zhuang et al., 2017, Zhuang et al., 2014), the extended finite element method (Lecampion, 2009, Mohammadnejad and Khoei, 2013), the explicit finite differences method (Fang and Harrison, 2002a, Fang and Harrison, 2002b, Li et al., 2015) and the boundary element method (Vásárhelyi & Bobet, 2000). In addition, methods based on remeshing algorithms enable accurate representation of curved crack paths (Areias et al., 2013, Areias et al., 2016, Fu et al., 2013). Discrete models have been based on the bonded particle method (Potyondy and Cundall, 2004, Yang et al., 2014, Manouchehrian et al., 2014), the distinct element method (Zhang & Sanderson, n.d.) and the discontinuous deformation analysis method (Pearce et al., 2000). Alternative methods, such as the meshfree cracking particles method (Rabczuk et al., 2010) and the peridynamics continuum method (Oterkus et al., 2017), do not require prescribed crack paths and allow for more complex fracture patterns as they occur in hydraulic fracturing.

In discrete-based models, the fractures are commonly regarded as mechanical discontinuities with a reduced dimension model for fluid flow in the fractures. These models are more realistic for simulating discontinuous

media, but they have the limitations of representing a subset of idealised straight fractures and not considering the intact rock permeability and damage to the intact rock between fractures. Continuum-based models require a representation of discrete fracture behaviour in an element cell by appropriate equivalent hydro-mechanical properties (Rutqvist et al., 2013, Rutqvist et al., 2009) and also a fine discretisation to capture details of the complex fracture network and stresses around the propagating fractures. Compared with discontinuous approaches, their main advantages are the representation of complex fracture networks with curved fractures and detailed geometry of both large and small fractures without the need of updating their topology, the representation of damage occurring in both fractures and intermediate rock between fractures, and the modelling with high accuracy of the hydro-mechanical behaviour of both rock matrix and the fractures, which can be sealed or filled with mineral materials. Thus, once the fracture propagates into the continuum medium, stress-induced changes in permeability and porosity can be included (Ji et al., 2009). By using an elastic-plastic and strain softening model, a continuum-based model may not be very effective in simulating fracture propagation because of large plastic zones around the fracture tips. However, it has been shown that a model based on degradation of the mechanical properties and stress distribution for the failure elements of the intact rock by tension and shear is effective for this purpose (Fang and Harrison, 2002a, Fang and Harrison, 2002b, Li et al., 2015).

To the authors' knowledge, no continuum-based model has been used in a detailed coupled hydro-mechanical study to understand the difference between propagation in a low-permeability medium of a single fracture and double parallel and non-parallel fractures under various stress conditions and different levels of fluid pore pressure. For our study of coupled hydro-mechanical effects as a function of increases in pore pressure, we consider two rock domains: the first with one fracture and the second with two adjacent parallel or non-parallel fractures. Changes in fluid pore pressure are assumed to be caused by a constant injection flow rate in a well that intersects one of the fractures.

The main objectives of this paper are (1) to verify or demonstrate the effectiveness of using a continuum mechanics-based model with an implemented elastic-brittle stress relationship to simulate the fracture propagation and stress concentrations around fracture tips, (2) to study how a single fracture propagates when it is subjected to hydraulic fracturing stimulation, (3) to evaluate changes in the pore pressure field and fracture permeability induced by coupled hydro-mechanical processes, (4) to analyse how the results are influenced by a nearby parallel or non-parallel fracture, and (5) to investigate the sensitivity of the results to input parameters to determine which parameters have the most significant influence on fracture propagation and linkage between nearby fractures during the hydraulic fracturing process. The paper is completed with some concluding remarks.

2. Problem definition

For our study, we choose to consider two rock domains, FD1 and FD2, each with dimensions 50 m × 50 m, which allows us to conduct a large number of simulations to explore the detailed coupled hydro-mechanical processes involved. The rock domains FD1 and FD2 consider one and two natural fractures, respectively (Fig. 1). In FD2, the left and right fractures are identified as fractures 1 and 2, respectively. In both rock domains, the length *2f* of the fractures is 2 m.

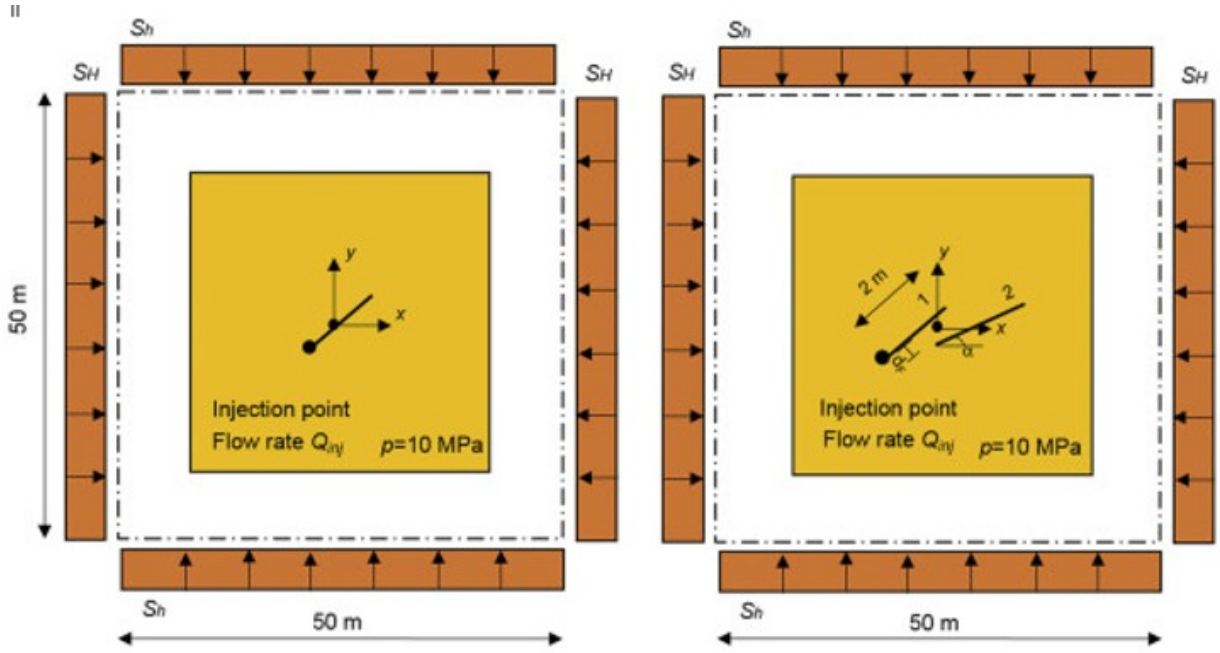

Fig. 1. Geometry of the rock domains FD1 (left) and FD2 (right), boundary loading and pore pressureconditions.

To study in detail the linkage between the two fractures in FD2, parallel and non-parallel fractures with different angles between them and the maximum horizontal boundary stress direction are considered. Thus, for the parallel fracture case, the fractures are assumed to be at angles α_1 and α_2 equal to 30°, 45° and 60°, and for non-parallel fracture cases, the angle α_1 of fracture 1 is equal to 45°, and the angle α_2 of fracture 2 is equal to 30° and 60°. The origin of the *x*- and *y*-axis system is located in the centre of the studied regions. In FD2, the closest distance d_F (Fig. 1) between the natural fractures is 0.25 m, with results of a sensitivity study to this parameter presented in Section 6.1.

Let us now assume that these rock domains are located at a depth of 1000 m. By assuming a vertical gradient of 0.027 MPa/m, the magnitude of the vertical stress component (S_v) at a depth of 1000 m is 27 MPa. A loading case is considered, in which the minimum horizontal boundary stress magnitude (S_h) is equal to the vertical stress magnitude (σ_v) and the ratio *SR* between the maximum horizontal S_H and minimum horizontal S_h boundary

stresses is 2 (Fig. 1). Further, a sensitivity test of the simulation results to the *SR* is conducted (see Section 6.2). Because the vertical dimension of the model is only 50 m, the vertical gradients of all stress components are neglected. The stresses are applied normal to the boundaries, which are free to move. No shear stresses are considered at the boundaries (Fig. 1). The results of our simulations show that because the boundary conditions are imposed far enough away, they do not influence the stresses around fractures or their propagation in the intact rock.

By assuming that the water table is located at the land surface and the fluid pore pressurehas a vertical gradient of 0.01 MPa/m, the fluid pore pressure p at a depth of 1000 m below the surface is 10 MPa. The pore pressure gradients in the x- and y-axis directions are neglected. All the boundaries are considered as closed to flow. Our simulations show that the results are not influenced by the flow boundary conditions.

We simulate water injection at a constant rate Q_{inj} for 2 h in one borehole penetrating the only fracture in FD1 and fracture 1 in FD2 (Fig. 1). The borehole is assumed to be vertical (perpendicular to FD1 and FD2). In this way, hydraulic fracturing is imposed in the single fracture in FD1 and in fracture 1 in FD2. After 2 h, the water injection is stopped, and the simulation continues for another hour.

3. Numerical approach

3.1. Finite-difference numerical model

To study the fracture propagation due to coupled hydro-mechanical effects as a result of hydraulic fracturing stimulation, a 3D model is desirable if at all possible. However, a global 3D model would be very large, and the necessary fine refinement close to the fracture would require a great computational effort. A 2D model is adequate from a mechanical perspective, particularly for investigating the fracture propagation, because this propagation is driven by the pore pressure build-up at the tip of the fractures, which can be simulated explicitly with a 2D model and an adequate injection rate. This injection rate should lead to a pore pressure at the fracture tip necessary to start fracture propagation, as observed in field experiments. A 2D finite-difference model is developed in FLAC3D (Itasca, 2012). This code is chosen because we would like to have the possibility of considering multiphase flow in future studies, and we already have the routines to couple FLAC3D with TOUGH2 (Pruess et al., 2011), which is a leading multiphase flow and transport simulator. The model is a square region with 50 m sides and a thickness of 1 m (Fig. 2). A plane strain analysis is performed. The mesh consists of 56,000 elements and is more refined in a square region 10 m by 10 m around the fractures, where the elements are squares with sides of 0.05 m (Fig. 2).

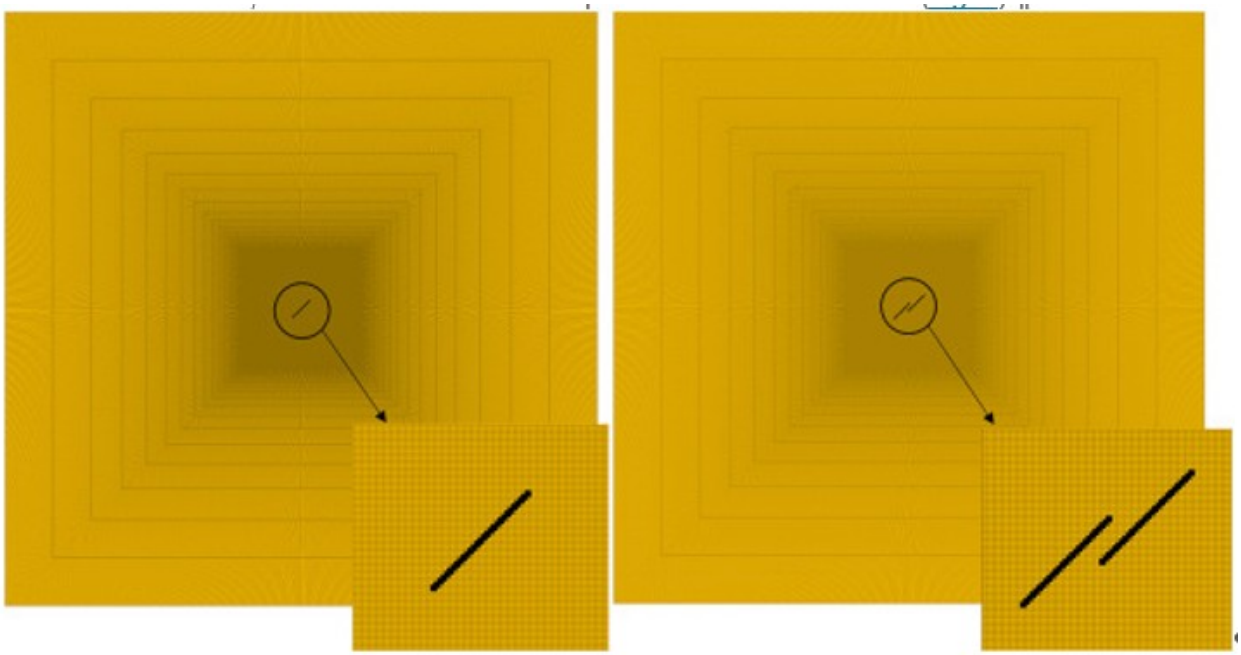

Fig. 2. Details of the mesh of the finite-difference model to study the hydro-mechanical behaviour of the rock domains FD1 (left) and FD2 (right) for the case of parallel fractures.

The natural fractures can be modelled as an equivalent solid material, in which the elastic modulus E_F of the elements intersected by a fracture trace is calculated according to the following equation ((Rutqvist et al., 2013, Rutqvist et al., 2009, Figueiredo et al., 2015)):

$$\frac{1}{E_F} = \frac{1}{E_R} + \frac{1}{k_n d} \quad (1)$$

where E_R is the elastic modulus of the intact rock, k_n is the fracture normal stiffness, and d is the element size (0.05 m).

In a continuum mechanics-based approach, the hydraulic behaviour of the fractures may be described in terms of the flow transmissivity and the normal and shear stiffness of the fractures. Laboratory experiments on single fractures show that the fracture transmissivity can be very sensitive to changes in stress normal to the fractures as well as to shear displacement. Thus, mechanically induced changes in the ability of the fracture to conduct fluid may be estimated using the cubic relations between flow along an open fracture and fracture aperture (Rutqvist and Stephansson, 2013, Cappa and Rutqvist, 2011):

$$T = \frac{b_h^3 \rho g}{12\mu} \quad (2)$$

where T is the fracture transmissivity, b_h is fracture aperture, ρ and μ are fluid density and viscosity, respectively, and g is the acceleration of gravity.

The permeability k_F of an element containing a fracture trace is related to the fracture aperture b_h by the cubic law:

$$k_f = \frac{b_h^3}{12d} \quad (3)$$

where d is element size (0.05 m).

3.2. Model parameters

The necessary model parameters are listed in Table 1. For the intact rock, a Mohr-Coulomb model with tension cut-off is used, in which the mechanical properties (elastic modulus E_R, Poisson's ratio ν_R, cohesion c_R, and friction angle φ_R) are characteristic of limestone rocks (Attewell and Farmer, 1976, Zhao, 2008). An elastic-brittle model is implemented in FLAC3D to describe the behaviour of the failure elements in the intact rock. This model is described in the next section. A tensile strength σ_{tR} of 5 MPa for the intact rock is assumed. An additional value of 10 MPa is considered, which is acceptable for intact limestone at a depth of 1000 m. The results show a decreased fracture extension when the tensile strength increases. In FD1, when the tensile strength increases from 5 to 10 MPa, the fracture propagation decreases by 0.7 m. In FD2, these decreases are 10 cm and 25 cm for fractures 1 and 2, respectively. However, the conclusions are similar to those reported in this paper. Regarding the hydraulic properties, the values of 10^{-18} m^2 and 0.001 are assigned to the permeability k_R and porosity ϕ_R of the intact rock, respectively, which are typical of limestone rocks. Further, the sensitivity of the results to the permeability of intact rock is investigated (see Section 6.3).

Table 1. FLAC3D model parameters.

Intact rock	Elastic modulus E_R (GPa)	20
	Poisson's ratio ν_R	0.2
	Tensile strength σ_{tR} (MPa)	5
	Cohesion c_R (MPa)	30
	Friction angle φ_R (°)	25
	Permeability k_R (m^2)	10^{-18}
	Porosity ϕ_R	0.001

Fractures	Elastic modulus E_F (GPa)	14.3
	Poisson's ratio ν_F	0.2
	Tensile strength σ_{tF} (MPa)	0
	Friction angle φ_F (°)	25
	Dilation angle ψ_F (°)	5
	Normal stiffness k_n (GPa/m)	1000
	Cohesion c_F (MPa)	0
	Aperture b_h (μm)	30
	Permeability k_F (m^2)	4.5×10^{-14}
	Porosity ϕ_F	0.01

The mechanical fracture behaviour is modelled with continuum elasto-plasticity using a Mohr-Coulomb constitutive model with tension cut-off. The mechanical properties of the fractures (Poisson's ratio ν_F, friction angle φ_F, dilation angle ψ_F, cohesion c_F, and fracture aperture b_h) are extracted from (Min et al., 2004). When the Mohr-Coulomb criterion is exceeded, plastic shear strain (and corresponding shear displacement) occurs along the fractures. The tensile strength σ_{tF} for fractures is assumed to be zero. The results of our simulations show low sensitivity to this parameter because tension failure occurs in the intact rock, and in the fractures, shear failure is the dominant mechanism. The fracture normal stiffness k_n is assumed to be 1000 GPa/m (Figueiredo et al., 2015). Additional values of 100 and 500 GPa/m are considered for the fracture normal stiffness k_n. For mechanical loading, the results show low sensitivity to this parameter. Based on a fracture aperture of 30 μm (see Table 1), Eqs. (2), (3) lead to a fracture transmissivity T of 2.2×10^{-8} m^2/s and permeability of fractures k_F of 4.5×10^{-14} m^2, respectively. The porosity ϕ_F of an element representing a fracture is assumed to be equal to 0.01 (Figueiredo et al., 2015).

In the theoretical study presented in this paper, we simulate water injection as representative of conditions that lead to propagation of existing fractures. We assume a 2D injection rate of approximately 4.0×10^{-4} m^3/s into a grid block of 0.0025 m^3. This injection results in a pressurisation rate to reach to a maximum injection pressure that is approximately 2.5 times the initial pore pressure.

3.3. Elastic-brittle model in the failure regions in the intact rock

The behaviour of the intact rock undergoing tension or shear failure may be simplified and represented by an elastic-brittle, elastic-strain softening (a combination of brittle and ductile) or elastic-ductile (plastic) mechanism. An elastic-plastic and strain softening model cannot effectively simulate the fracture propagation because large plastic zones appear around the fracture tips. An elastic-brittle stress-strain relation, based on degradation of the mechanical properties and consequent stress distribution for the failure elements by tension and shear, has been shown to be more effective for this purpose (Fang and Harrison, 2002a, Fang and Harrison, 2002b, Li et al., 2015). In this model, the failure of an element causes disturbance of the local stress field, which may lead to progressive failure of surrounding elements.

In this model, for the elements in the intact rock that undergo yield tensile strength, stiffness and strength properties are degraded according to a damage variable D. This variable can be expressed by the following equations (Li et al., 2015):

$$D = \begin{cases} 0, \varepsilon < \varepsilon_{t0} \\ 1 - \frac{\sigma_{t,res}}{E \cdot \varepsilon}, \varepsilon_{t0} \le \varepsilon \le \varepsilon_{tu} \\ 1, \varepsilon > \varepsilon_{tu} \end{cases} \tag{4}$$

$$\sigma_{t,res} = \eta \sigma_t \tag{5}$$

$$\varepsilon = \sqrt{(\varepsilon_1)^2 + (\varepsilon_2)^2 + (\varepsilon_3)^2} \tag{6}$$

where $\sigma_{t,res}$ is the residual tensile strength, E and σ_t are the elastic modulus and tensile strength of the intact rock, respectively (Table 1), η is the residual strength coefficient, ε_{t0} is the initial damage threshold, ε_{tu} is the limit of tensile strength, and ε_1, ε_2 and ε_3 are the three principal strains.

For the elements of the intact rock subjected to shear failure, the damage variable D can be expressed as follows (Li et al., 2015):

$$D = \begin{cases} 0, \varepsilon_s < \varepsilon_{s0} \\ 1 - \frac{\tau_{s,res}}{\varepsilon_s \cdot E}, \varepsilon_s \ge \varepsilon_{s0} \end{cases} \tag{7}$$

where E is the elastic modulus, $\tau_{s,res}$ is the residual strength of shear damage, ε_{s0} is the strain threshold of shear damage, and ε_s is the shear strain.

This model was implemented in a finite difference scheme. In our case, it was found that shear failure did not occur in the intact rock where tension failure was the dominant mechanism. In these regions, the stiffness and strength properties were degraded. Stiffness degradation was implemented by simply updating the elastic modulus E in the stress-strain calculations, and strength degradation was modelled by reducing the tensile strength σ_t and the cohesion c of the intact rock. The friction angle was held invariant (Li et al., 2015). The corrected values for the elastic modulus E_{corr}, tensile strength $\sigma_{t,corr}$ and cohesion c_{corr} are given by the following equations:

$$E_{corr} = E - (E - E_{res}) \times D \quad (8)$$

$$\sigma_{t,corr} = \sigma_t - (\sigma_t - \sigma_{t,res}) \times D \quad (9)$$

$$c_{corr} = c - (c - c_{res}) \times D \quad (10)$$

where E_{res}, $\sigma_{t,res}$ and c_{res} are the residual values of the elastic modulus, tensile strength and cohesion, respectively. In our simulations, the initial values of the elastic modulus, tensile strength and cohesion (Table 1) were reduced to one percent of the original values (Li et al., 2015). This process enabled our model to obtain a good fit for fracture extension with the analytical solutions when the rock domain was subjected to differential boundary stresses, as shown in Section 4.

In the original fractures, shear failure is the dominant mechanism. The elements that represent them undergo shear failure after very small shear strains because they have null cohesion. Consequently, for those elements, the stiffness is not degraded, and the elastic modulus is given by Eq. (1).

3.4. Permeability changes in the natural fractures and tension failure regions

In fractured rock masses, effective stresses (which include the effect of fluid pore pressure) induce changes in hydraulic properties such as the permeability and porosity. In natural fractures, the initial values of porosity and permeability are corrected by taking into account changes in volumetric strains (Cappa & Rutqvist, 2011), which are defined as the ratios of the change in volume of the fracture elements to their original volume. For this purpose, a model developed and applied by (Chin et al., 2000) to consider permeability changes in petroleum reservoirs is used. This model first relates the porosity ϕ at a given stress to the isotropic volumetric strain variation ε_v in the fracture elements and then the permeability k at a given stress to changes in porosity, according to the following equations:

$$\phi = 1 - (1 - \phi_i)\exp(-\varepsilon_v) \quad (11)$$

$$k = k_i \left(\frac{\phi}{\phi_i}\right)^n \quad (12)$$

where ϕ_i is the initial porosity, k_i is the initial permeability and n is a power law exponent.

With the changes in volumetric strains resulting from changes in the normal stress of fractures, changes in fracture apertures are considered: if the compressive stress normal to the fractures decreases, the fracture aperture increases, and the compressive volumetric strains decrease. Volumetric strains include elastic and plastic components. The elastic component is originated by elastic shear deformation until the Mohr-Coulomb criterion is reached. After this criterion is reached, shear failure occurs, and variations in the volumetric strains include the effects of plastic shear deformation and associated shear dilation. Shear dilation leads to an increase in the fracture aperture and a subsequent increase of porosity and permeability of the fractures.

The empirical relation between permeability and porosity expressed in Eq. (12) has been shown to be widely applicable to geological materials. Although the exponent n can vary between 3 and 25 for consolidated geological materials (Rinaldi et al., 2014), we have set the exponent to 3, based on a cubic variation of the permeability with the aperture and porosity of the elements intersected by the fracture trace (Witherspoon et al., 1980):

$$\frac{k}{k_i} = \left(\frac{b_h}{b_{hi}}\right)^3 = \left(\frac{\phi \cdot d}{\phi_i \cdot d}\right)^3 = \left(\frac{\phi}{\phi_i}\right)^3 \quad (13)$$

where b_{hi} is the initial aperture of the fractures.

The regions that fail by tension in the intact rock are considered to be similar to natural fractures. When the elements of the intact rock fail by tension, they are assigned the same initial values for porosity and permeability as those elements that represent the natural fractures. Then, these initial values are updated according to Eqs. (11), (12) to account for the stress-induced changes in porosity and permeability (Cappa & Rutqvist, 2011). In this way, the extension of fractures is modelled. It is found that the maximum increase in the initial permeability of the tension failure regions is two orders of magnitude. Further, a sensitivity test of results to the permeability of the tension failure regions is conducted (see Section 6.4).

3.5. Coupled hydro-mechanical calculation

A mechanical analysis is performed by considering the boundary stresses S_H and S_h and the initial fluid pore pressure p of 10 MPa. After mechanical equilibrium is reached, a flow analysis is completed to calculate changes in

the pore pressure field resulting from water injection into the fracture (Fig. 1) with a constant flow rate Q_{inj} during a 2 h period. At 2 h of injection, water injection is stopped. The increase in the fluid pore pressure in the fracture and surrounding intact rock leads to a decrease in the effective stress. In the regions of intact rock where the tensile stresses exceed the tensile strength, tension failure occurs. Then, a mechanical analysis is performed to calculate stress field-induced changes in porosity and permeability. The post-failure values of porosity and permeability of these tension failure regions are set to the respective values considered for natural fractures. Next, changes in porosity and permeability in the natural fractures and tension failure regions are considered as a function of the volumetric strains, as described in Section 3.4. The coupled hydro-mechanical analysis is sequential and steps forward in time. In each time step of the transient flow calculation, a quasi-static mechanical analysis is conducted to calculate stress-induced changes in permeability. The analysis is performed for a period of 3 h (shut-in occurs after 2 h of injection).

4. Verification of the model for fracture propagation

This section aims to verify the use of our continuum mechanics model based on FLAC3D to simulate the fracture propagation in intact rock with a single fracture and to reproduce the stresses close to the fracture. To study fracture propagation, the rock domain FD1 is considered and differential boundary stresses S_H and S_h are applied (Fig. 1). It is assumed that the fracture has no filling material and is completely open with no fracture surface contacts (no stiffness or stress transfer through surface contacts). The compressive maximum boundary stress S_H is set to 40 MPa (Fig. 1), and the stress ratios SR between the maximum horizontal S_H and minimum horizontal S_h boundary stresses is considered to have four alternative values: 4, 5, 6.7, and 10. In the intact rock, the model parameters presented in Table 1 are used. Meshes with square elements of 2, 5 and 10 cm sides around the fracture are studied.

Fig. 3a shows the fracture propagation obtained with our continuum mechanics-based model by using a mesh with square elements of 5 cm sides. The figure shows that at the tip of the pre-existing fracture, the fracture propagation is not confined to a straight row of fractures, because of the formation of curved wing crack initially. Then, at a certain distance away from the fracture tip, the fracture propagates in the direction perpendicular to the minimum principal stress direction.

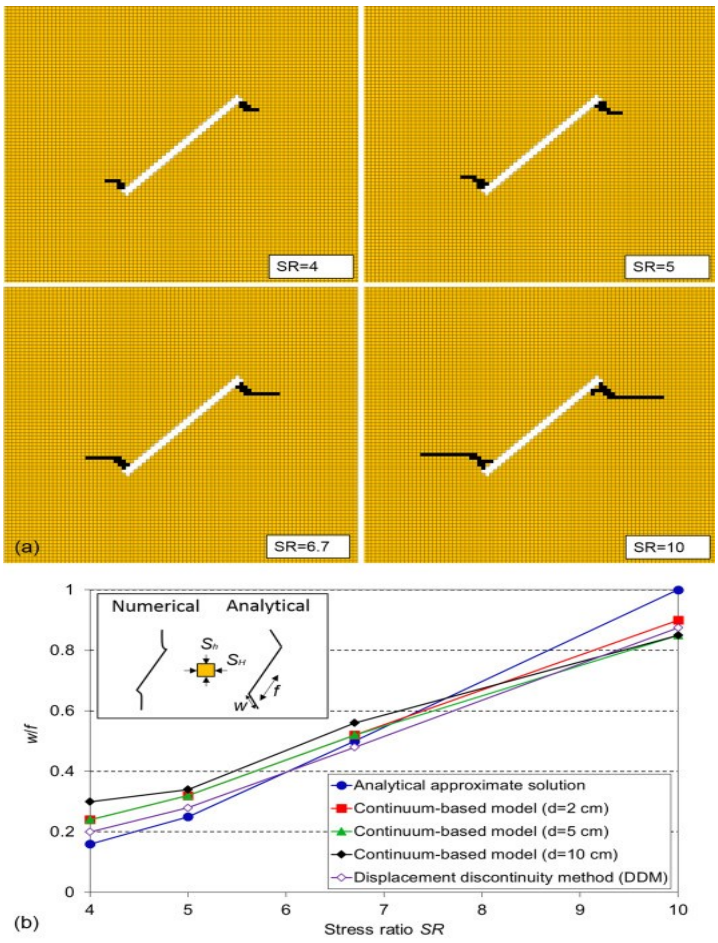

Fig. 3. (a) Fracture propagation obtained with the continuum-based model for an element size *d* equal to 5 cm for four different *SR* values, where *SR* is the ratio of the maximum horizontal S_H to the minimum horizontal S_h boundary stresses; (b) Variation of the dimensionless length *w*/*f* of the tension cracks as a function of the stress ratio *SR*. The value of *w*/*f* is measured along the curved fracture propagation from our continuum mechanics-based model and the displacement discontinuity method (DDM), whereas it is measured along a straight path in the analytical approximation. Data of the DDM method and the analytical approximate solution are taken from Mutlu & Pollard (2008).

Fig. 3b shows, for the three degrees of mesh refinement, a comparison of the length *w* of the fracture extension (wing crack by tension), normalised by the half-length *f* of the fracture with that obtained by analytical approximation for an infinite elastic medium, and by a 2D displacement discontinuity method (DDM), presented in Mutlu & Pollard (2008). Analytical results are obtained by assuming that the propagating fracture follows a straight path, whereas the results of our approach and DDM method are obtained by allowing the fracture propagation to propagate along a curved path. Our results show that the fracture propagations obtained for the three degrees of mesh refinement are very similar. For all the stress ratio values, the maximum difference for the ratio *w*/*f* obtained with the three meshes is found to be smaller than 0.06. The comparison of the ratio *w*/*f* values obtained with our continuum mechanics-based model and the analytical solution shows that the ratio given by the analytical solution is less than that estimated from our model by about 0.08 for *SR* = 4, 0.07 for *SR* = 5, 0.02 for

SR = 6.7, and 0.15 for SR = 10. These differences are not surprising since the analytical approximation is restricted to the simplified case of straight wing cracks, whereas the numerical model simulates fracture propagation along a curved path. These differences are of the same order of magnitude that those observed between the analytical approximation and the results of the displacement discontinuity method. These differences are acceptable because of the assumptions inherent to each numerical method. In DDM method, the pre-existing fracture, with zero thickness, is approximated with very short displacement discontinuity elements, and the intact rock is assumed to be elastic. In our continuum-based model with an elastic-brittle stress relation based on degradation of material properties, the mesh is orthogonal, the pre-existing fracture is open with no fracture surface contacts, and furthermore initial and residual values for the tensile strength need to be assigned to the intact rock. These assumptions cause slight differences in the curvature of the wing crack which in turn leads to differences in the wing crack length between the two numerical models.

To check whether the mesh resolution is sufficient to obtain a good estimate of the stresses close to the fractures developed in the elastic regime, a very simple model with one vertical fracture of a length $2f$ equal to 2 m was considered. A stress S_H of 40 MPa was applied in the boundaries perpendicular to the x-axis (Fig. 4a). The variation of the ratio between fracture normal stress σ_{xx} and boundary stress S_H as a function of distance $r/2f$ along the lines $x = 0$ and $y = 0$ away from the fracture was obtained in the centre of the mesh elements of the intact rock and compared with the analytical solution presented in (Pollard & Segall, 1987). The results of this comparison obtained for a mesh with elements of 2, 5 and 10 cm sides around the fracture are shown in Fig. 4b, c and d. The results show that for the element which is the closest to the fracture tip, the differences between the solution provided by (Pollard & Segall, 1987) and our continuum mechanics-based model are approximately 9%, 10% and 35% for d equal to 2, 5 and 10 cm sides, respectively. However, these differences occur in the very steep part of the curve and Fig. 4b, c and d show very good agreement visually. The agreement between analytical solution and our model results is very good for the stress values away from the fracture tip.

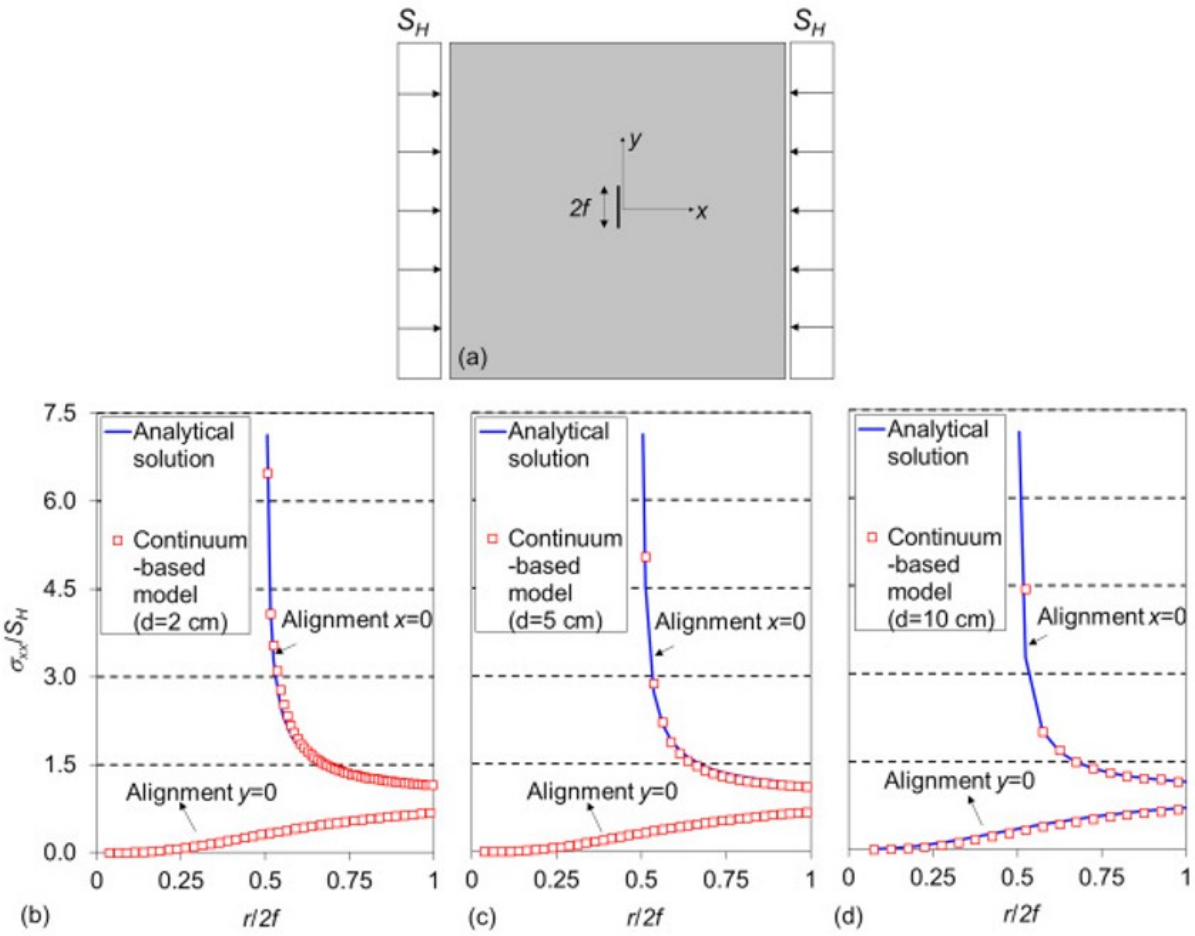

Fig. 4. (a) Geometry and boundary conditions of the model used to study the behaviour of a single fracture with length *2f*; (b), (c) and (d) variation of the dimensionless fracture normal stress σ_{xx}/S_H as a function of the dimensionless distance *r/2f* away from the fracture along the lines $x = 0$ and $y = 0$ (*d* is the element size).

This verification study enables us to conclude that, away from the fracture tip, the stress distributions are accurately represented by the three meshes. Very close to the fracture tip, the calculated stress concentrations are better represented by meshes with square elements of 2 and 5 cm sides, which provide similar accuracy. Because the more refined mesh implies a significant additional computational effort, the results presented in Sections 5 and 6 were obtained for the mesh with square elements having 5 cm sides around the fractures.

In contrast to this verification study, for our present investigation, fractures with filling material or with stress transfer through surface contacts are considered. This scenario is more realistic because it enables the possibility of considering changes in fracture aperturecaused by changes in the stress normal to the fractures. In such scenarios, close to the fracture tip, the stress concentrations are much smaller than those presented in Fig. 4; hence, there is no need to capture the stress singularity in our elasto-plastic continuum mechanics-based model.

5. Results

In this section, the results for tension failure regions and changes in fluid pore pressure and in fracture permeability are presented for a base case, in which the ratio SR between the magnitudes of the maximum and minimum boundary stresses, the permeability k_R of the intact rock, the initial permeability k_{TF} of the tension failure regions and the closest distance d_F between natural fractures in FD2 are fixed. The sensitivity of results to these key input parameters is investigated in Section 6.

5.1. Results for tension failure regions

Fig. 5 shows the regions that fail by tension in the intact rock for rock domains FD1 and FD2, obtained at 1.5, 2 and 3 h for parallel fractures with angles $\alpha_1 = \alpha_2 = 45°$. An interesting aspect is that the ratio of 2 between the magnitudes of boundary stresses is too small to lead to formation of wing cracks from mechanical effects alone, as observed in Fig. 3. In addition, in our study, the fractures have stiffness or shear transfer through fracture surface contacts, and consequently, their extension is parallel to the maximum principal stress direction from the moment of crack initiation, as shown by (Vásárhelyi & Bobet, 2000). At 1.5 and 2 h of injection, the results show that in FD1, the fracture extensions are approximately 0.35 and 1.75 m, respectively. In FD2, fractures 1 and 2 (Fig. 1) are already connected at 1.5 h of injection. At 2 h of injection, their extension (away from the connected region) is 35 cm, which is significantly smaller than in FD1. In addition, fracture 1 does not extend beyond fracture 2. This effect occurs because fracture 2 is inclined to the principal stress directions and has softer properties from those of the surrounding intact rock. When the two fractures connect, the pore pressure decreases and becomes smaller than the minimum pressure necessary to continue propagating the fracture (see Section 5.2). In FD1, at 3 h, the fracture propagates approximately 2.25 m longer and is still propagating. In the case of FD2, the two fractures propagate only 0.15 m after the shut-in at 2 h of injection. This difference is because, in FD1, the fluid pore pressure in the fracture is larger than that in FD2. This result is explained with more detail in the next section.

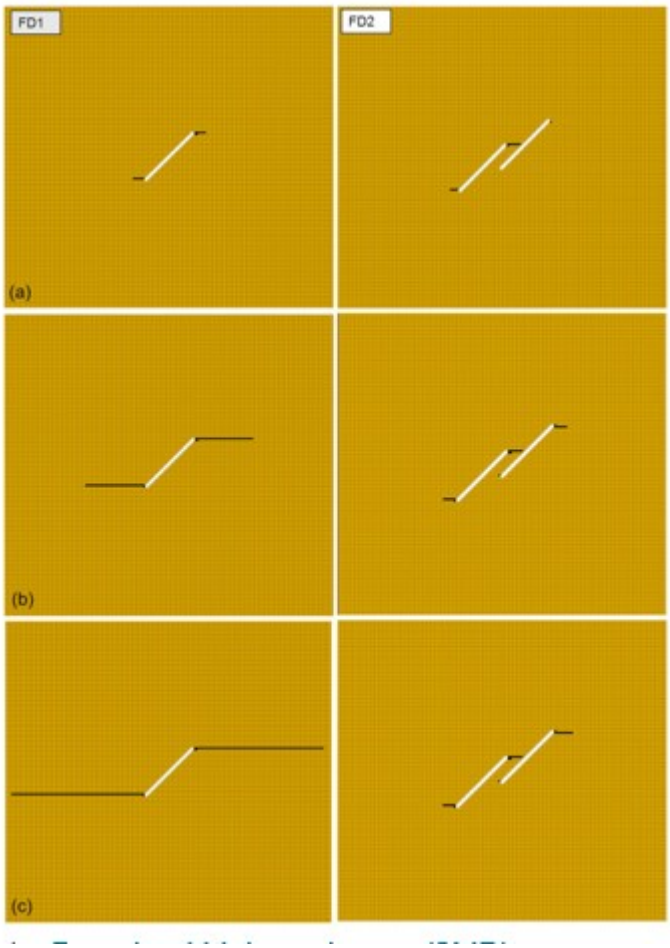

Fig. 5. Tension failure regions in rock domains FD1 (left) and FD2 with parallel fractures (right) at (a) 1.5 h, (b) 2 h, and (c) 3 h (results obtained for fracture angles $\alpha_1 = \alpha_2 = 45°$).

Let us now consider the rock domain FD2 and the 2 h injection period. Fig. 6 shows those failure regions for parallel fractures inclined at angles $\alpha_1 = \alpha_2 = 30°$ and $\alpha_1 = \alpha_2 = 60°$ and non-parallel fractures inclined at angles $\alpha_1 = 45°$ and $\alpha_2 = 30°$ or $\alpha_2 = 60°$. In the results obtained for parallel fractures with $\alpha_1 = \alpha_2 = 30°$, the extension of both fractures (away from the connection zone) is 30 cm, which is 5 cm less than that obtained for fracture angles $\alpha_1 = \alpha_2 = 45°$. When $\alpha_1 = \alpha_2 = 60°$, the fractures connect, but their propagation is small because for this geometry, the fractures are sub-perpendicular to the horizontal direction, which is the maximum principal stress direction. For the case of non-parallel fractures, when α_2 decreases from 45° to 30°, the extension (away from the connected region) of the pressurised fracture (fracture 1) increases approximately 0.5 m. When α_2 increases from 45° to 60°, that fracture extension decreases approximately 0.4 m. For α_2 equal to 60°, the non-pressurised fracture (fracture 2) does not propagate. These results are explained in Section 5.2.

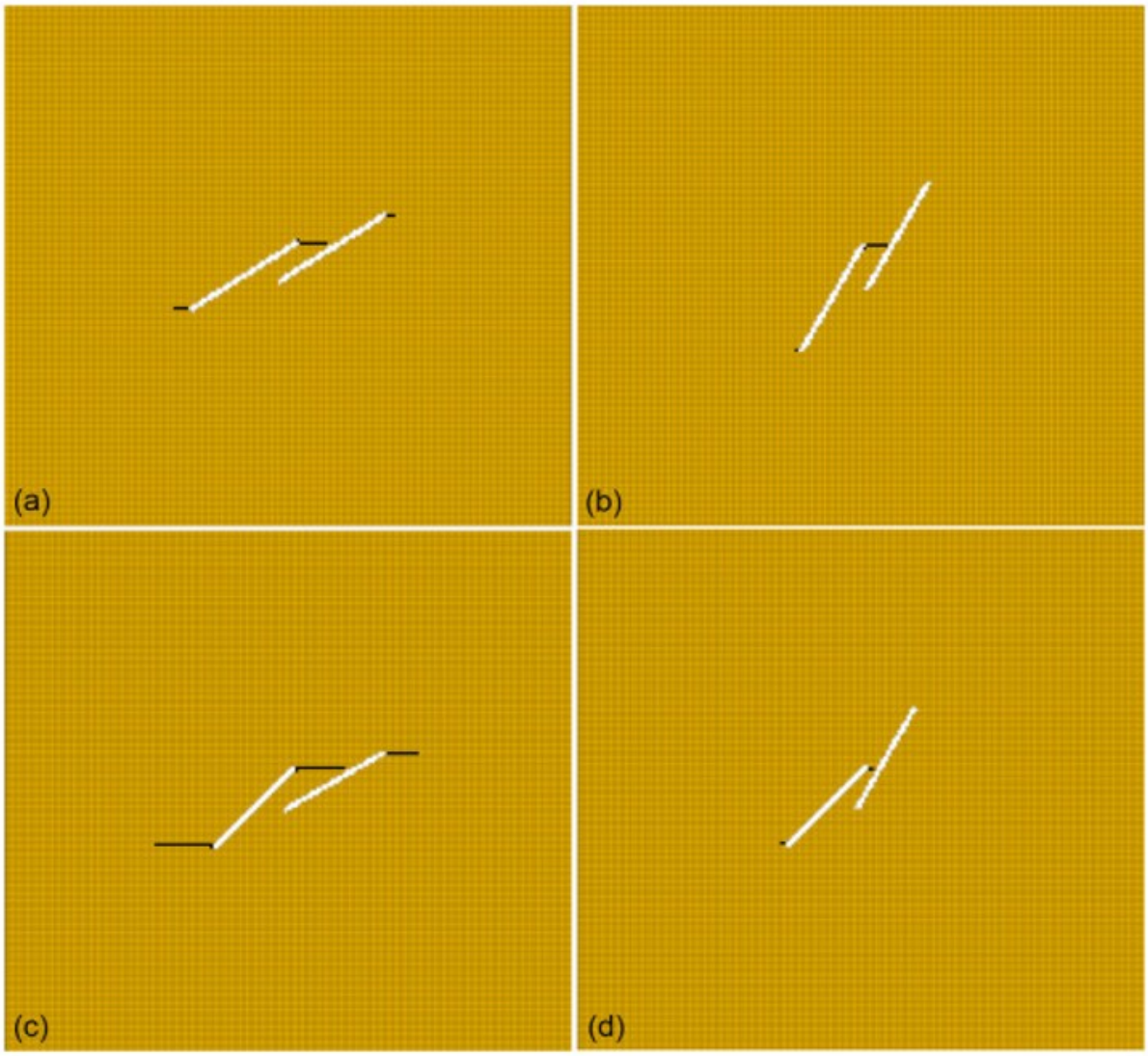

Fig. 6. Tension failure regions in rock domain FD2 for fracture angles (a) $\alpha_1 = \alpha_2 = 30°$ (parallel); (b) $\alpha_1 = \alpha_2 = 60°$ (parallel); (c) $\alpha_1 = 45°$ and $\alpha_2 = 30°$ (non-parallel); and (d) $\alpha_1 = 45°$ and $\alpha_2 = 60°$ (non-parallel) (results obtained at 2 h of injection).

5.2. Changes in fluid pore pressure

In this section, changes in the fluid pore pressure due to coupled hydro-mechanical effects are analysed. Fig. 7 shows the contours of the fluid pore pressure fields obtained in rock domains FD1 and FD2 after 1.5 h, 2 h (end of injection) and 3 h (after 1 h of shut-in), when the two fractures are parallel and have angles $\alpha_1 = \alpha_2 = 45°$. Fig. 8 shows the variations of the fluid pore pressure with time in the centre of the fractures for the rock domains FD1 and FD2.

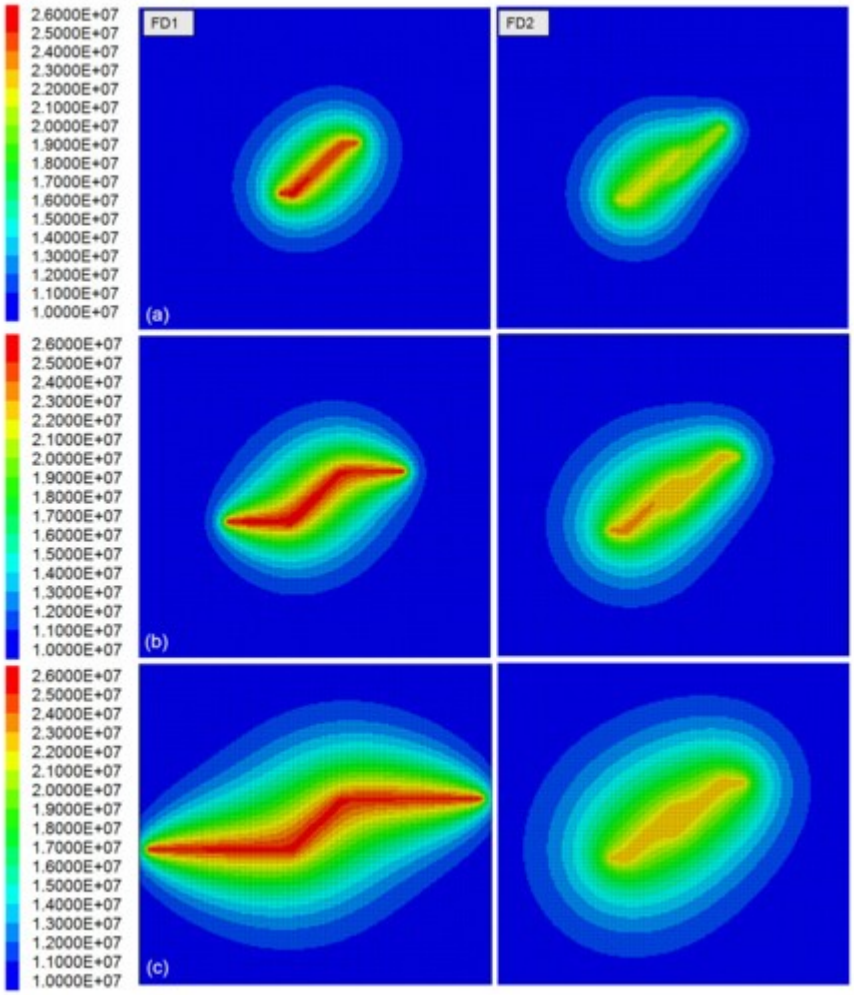

Fig. 7. Fluid pore pressure field (Pa) obtained over rock domains FD1 (left) and FD2 with parallel fractures (right) for at (a) 1.5 h, (b) 2 h, and (c) 3 h (results obtained for fracture angles $\alpha_1 = \alpha_2 = 45°$).

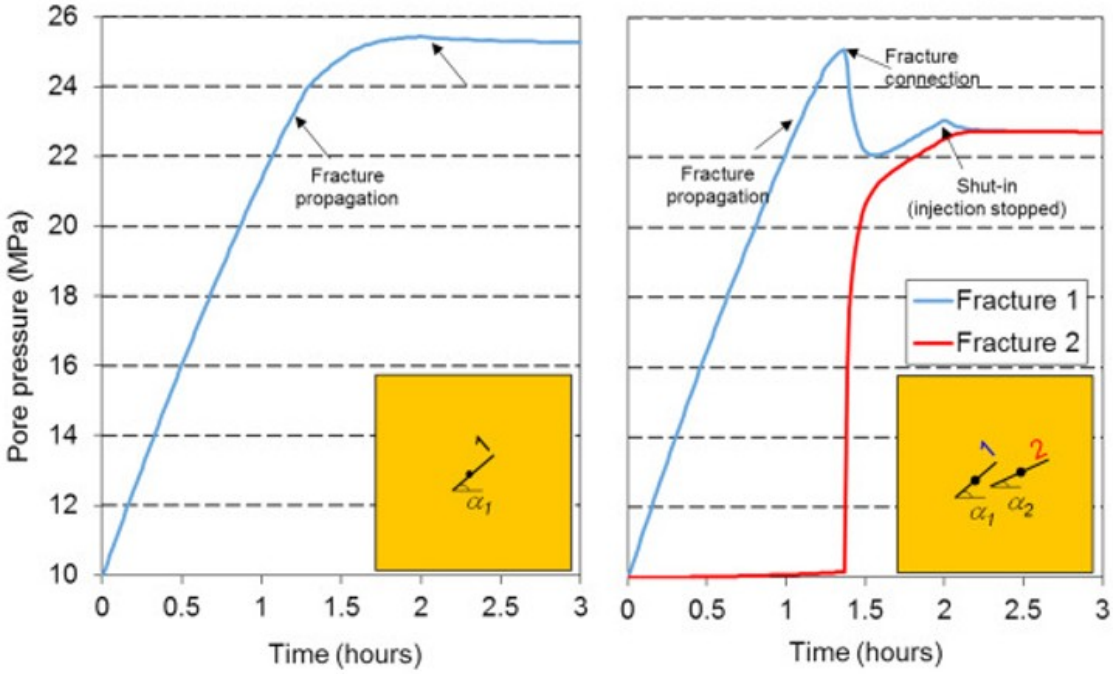

Fig. 8. Variation with time (hours) of the fluid pore pressure (MPa) in the centre of fractures for the rock domains FD1 (left) and FD2 (right) with parallel fractures (results obtained for fracture angles $\alpha_1 = \alpha_2 = 45°$).

The results show that the variations of fluid pore pressure with time in rock domains FD1 and FD2 are different. In FD1, this relationship is approximately linear until approximately 1 h. The reason why this relation is not perfectly linear is because of the diffusion of the fluid pore pressure into the intact rock (Fig. 7). For a fluid pore pressure of approximately 23 MPa, the fracture starts to propagate, and the rate of fluid pore pressure build-up decreases with time. The fluid pore pressure necessary to initiate the fracture propagation is smaller than the minimum boundary stress magnitude (27 MPa). This difference occurs because the fracture has different properties from those of the surrounding intact rock, so that the minimum principal stress around the fracture tip becomes slightly smaller than the minimum boundary stress magnitude when differential boundary stresses are applied. The fracture starts to propagate when the tensile stress caused by the increase of pore pressure exceeds the tensile strength of the intact rock around the fracture. At that instant, the pore pressure at the fracture centre is larger than that at the tips. As the fracture propagates, the elements that fail in tension have an increase in permeability (see Section 5.3). This event leads to fluid penetration into the adjacent elements and a consequent increase in fluid pore pressure (Fig. 7), which in turn leads to tension failure in these elements. In this way, during the hydro-mechanical calculation, the fluid pore pressure diffusion follows the extension of the fractures (Fig. 5, Fig. 7). At 1.5 and 2 h of injection, the maximum fluid pore pressures in the fracture are 24.8 and 25.4 MPa, respectively. After shut-in, the pressure

decrease is very small (less than 0.1 MPa), and the fracture propagates significantly by 3 h (Fig. 5).

In FD2, the fractures start to propagate at approximately the same fluid pore pressure as observed in FD1 (23 MPa). In fracture 1, the fluid pore pressure increases with time until the two fractures connect, which occurs after approximately 80 min and for a fluid pore pressure of approximately 25.5 MPa (Fig. 8). Before the two fractures connect, there is a small increase of fluid pore pressure in fracture 2 (less than 0.2 MPa) due to the low permeability of the intact rock. When the fractures connect, the fluid pore pressures in fractures 1 and 2 suddenly decrease and increase, respectively. At 1.5 h of injection (10 min after the fractures connect), the fluid pore pressures in fractures 1 and 2 are approximately 22 and 21 MPa, respectively. After that, the fluid pore pressure continues to increase in both fractures because the increase in fracture permeability is not significant (see Section 5.3). As a result of pore pressure increase, fracture 2 starts to propagate (Fig. 5). At 2 h of injection, the fluid pore pressures in fractures 1 and 2 are approximately 23 and 22.5 MPa, respectively. One hour after shut-in, the pore pressure in both fractures is significantly smaller than that observed in FD1 (approximately 22.8 MPa), and the fractures propagate only a further 0.15 m.

Fig. 9 shows the time evolution of pore pressure for parallel fractures having angles $\alpha_1 = \alpha_2 = 30°$ and $\alpha_1 = \alpha_2 = 60°$ and for non-parallel fractures in which $\alpha_1 = 45°$ and $\alpha_2 = 30°$ or $\alpha_2 = 60°$. For parallel fractures, the results obtained for $\alpha_1 = \alpha_2 = 30°$ show that the fractures connect when fluid pore pressure is similar to that obtained for $\alpha_1 = \alpha_2 = 45°$ (Fig. 8). At 2 h of injection, the fluid pore pressure in the two fractures is approximately equal to 23 MPa. When $\alpha_1 = \alpha_2 = 60°$, the fluid pore pressure increases mainly in fracture 1 until the fractures connect for a maximum value of approximately 31.5 MPa, which is 6 MPa larger than that obtained when $\alpha_1 = \alpha_2 = 30°$ or $\alpha_1 = \alpha_2 = 45°$ (Fig. 8, Fig. 9). For non-parallel fractures, the results show that when the angle between the non-pressurised fracture (fracture 2) and the maximum boundary stress direction increases, the distance between the tip of the pressurised fracture and the neighbouring fracture decreases, and as a consequence, the time necessary for the fractures to connect decreases. In this way, when the fractures connect at an earlier instant of time, the increase in the initial pore pressure is less, and the fractures propagate less (Fig. 6). The controlling factor for fracture propagation appears to be the separation between the tips of the pressurised fracture 1 and the neighbouring fracture 2.

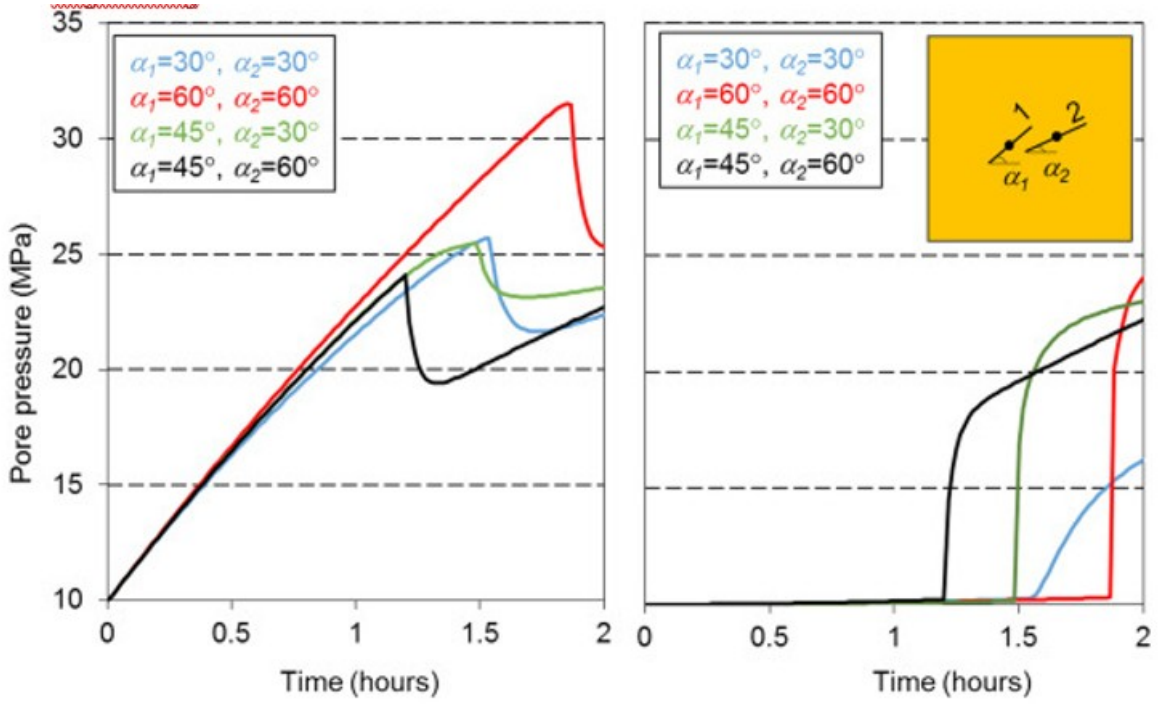

Fig. 9. Variation with time (hours) of the pore pressure (MPa) in the centre of the fractures 1 (left) and 2 (right) in rock domain FD2 obtained for fracture angles α_1 and α_2 (results obtained at 2 h of injection).

5.3. Changes in fracture permeability

In this section, changes in permeability of the natural fractures are analysed. Fig. 10 shows the variation with time of the permeability in the centre (points A and D) and tips (points B, C and E) of the fractures. These results are obtained for parallel fractures with angles $\alpha_1 = \alpha_2 = 45°$.

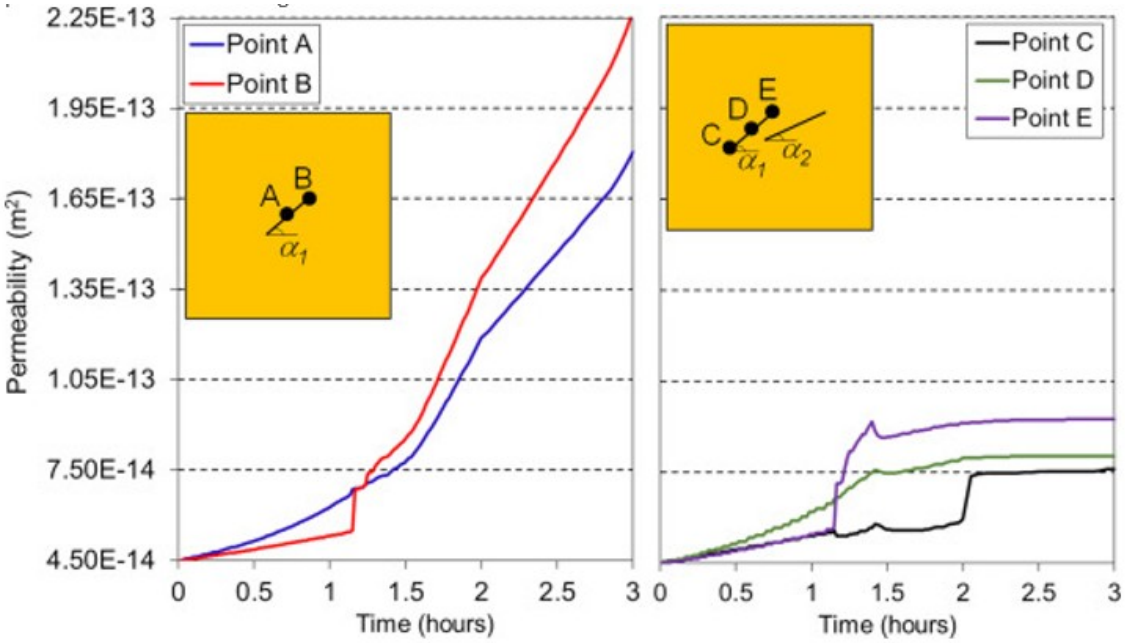

Fig. 10. Variation with time (hours) of the fracture permeability (m^2) in the centre (points A and D) and tips (points B, C and E) of the fractures for the rock domains FD1 (left) and FD2 (right) (results obtained for fracture angles $\alpha_1 = \alpha_2 = 45°$).

In rock domain FD1, before the fracture propagation initiates, changes in permeability in the centre of the fracture (point A) are slightly higher than those at the tip (point B). When the fracture begins to propagate, at approximately 70 min after injection is started, the increase in permeability at the fracture tip (point B) is larger than in the centre (point A). At 1.5 h of injection, the permeability of the centre of the fracture (point A) is approximately 1.7 times the initial value. At 2 h of injection, the maximum fracture permeability (point A) is approximately 3 times the initial value. After shut-in, the fracture continues to propagate and hence, the permeability continues to increase. At 3 h, the maximum fracture permeability (point B) is approximately 5 times the initial value. In FD2, changes in fracture permeability are less significant than in FD1 because when the two fractures become connected, the fluid pore pressure decreases (Fig. 8) and as a result, changes in fracture apertures are smaller. After the fractures connect, the permeability at point E, located at the tip of the fracture, is slightly higher than at the centre (point D), as observed in the case of FD1. At 2 h of injection, at points D and E, the permeabilities at points D and E are approximately 1.8 and 2.0 times the initial value, respectively. The fracture permeability remains practically constant after shut-in because fracture propagation is very small (Fig. 8).

Fig. 11 shows the time evolution of permeability in the centre of the fractures for parallel fractures having angles $\alpha_1 = \alpha_2 = 30°$ and $\alpha_1 = \alpha_2 = 60°$ and for non-parallel fractures in which $\alpha_1 = 45°$ and $\alpha_2 = 30°$ or $\alpha_2 = 60°$. For parallel fractures, the results obtained for $\alpha_1 = \alpha_2 = 30°$ show that the permeability changes are similar to those obtained with $\alpha_1 = \alpha_2 = 45°$ (Fig. 10). As a result, the time evolutions of pore pressure obtained with $\alpha_1 = \alpha_2 = 30°$ and $\alpha_1 = \alpha_2 = 45°$ are similar (Fig. 8, Fig. 9). When $\alpha_1 = \alpha_2 = 60°$, changes in permeability are smaller than in the other analysed cases. For this case, although the pore pressure in the centre of fracture 1 is larger than that in the other cases (Fig. 8, Fig. 9), the fracture propagation decreases because it is sub-perpendicular to the maximum principal direction (Fig. 6). For the case of non-parallel fractures, when α_2 increases from 30° to 60°, the permeability decreases because the fractures connect at an earlier time, and as a result, the increase in the pore pressure is less (Fig. 9), and the fracture propagation decreases.

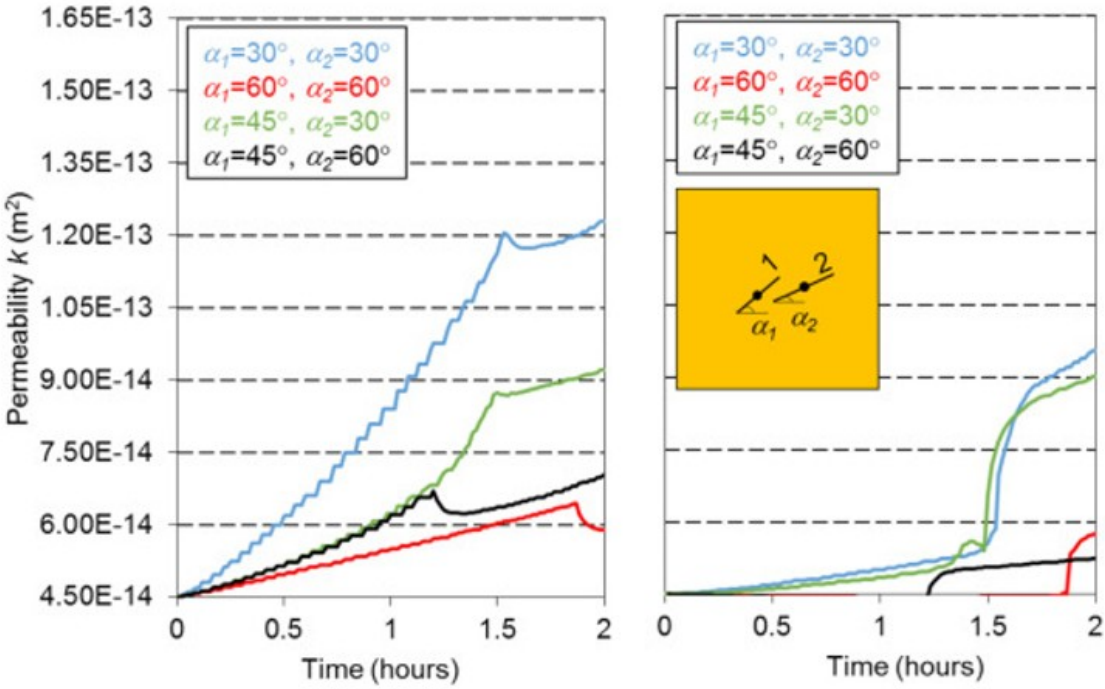

Fig. 11. Variation with time (hours) of the permeability (m^2) of in the centre of the fractures 1 (left) and 2 (right) in rock domain FD2 obtained for fracture angles α_1 and α_2 (results obtained at 2 h of injection).

6. Sensitivity of results to input parameters

This section presents the results of a sensitivity analysis to study the influence of the distance d_F between the natural fractures, the ratio SR between the magnitude of the maximum and minimum boundary stresses, the permeability k_R of the intact rock and the initial permeability k_{TF} of the tension failure regions on the simulation results. The values of these key parameters used in the sensitivity study are presented in Table 2 together with those used for the base case. In this analysis, only rock domain FD2 with parallel fractures inclined at an angle of 45° and the period up to shut-in (2 h) are considered.

Table 2. Values of the key parameters considered in the base case and sensitivity study.

Key parameter	**Parameter value**	
	Base case	**Sensitivity study**
Distance d_F (m)	0.25	0.50, 0.75
Stress ratio SR	2	1, 3
Permeability k_R (m^2)	10^{-18}	10^{-17} 10^{-16}

Key parameter	Parameter value	
	Base case	**Sensitivity study**
Initial fracture permeability k_{TF} (m^2)	4.5×10^{-14}	4.5×10^{-15} 4.5×10^{-16} 4.5×10^{-18}

6.1. Effect of the distance d_F between the natural fractures

Fig. 12 shows the fracture extensions and the curves of the variation of fluid pore pressurewith time in the centre of fractures 1 and 2, obtained for a distance d_F between natural fractures of 0.5 m and 0.75 m. The results are compared with those presented in section 5, obtained for d equal to 0.25 m. When d increases from 0.25 m to 0.5 m, the fracture extension (away from the connection region) increases approximately 0.8 m. When d is 0.75 m, the propagation of fracture 1 is similar to that obtained in the single fracture case. This comparison shows that, as d increases, the time necessary for fractures to connect slightly increases, which leads to a major increase in pore pressure and propagation of the pressurised fracture. This situation results in a larger difference in fracture propagation and fluid pore pressure in the two fractures. In addition, as d increases, the effects caused by the linkage between the two fractures decrease.

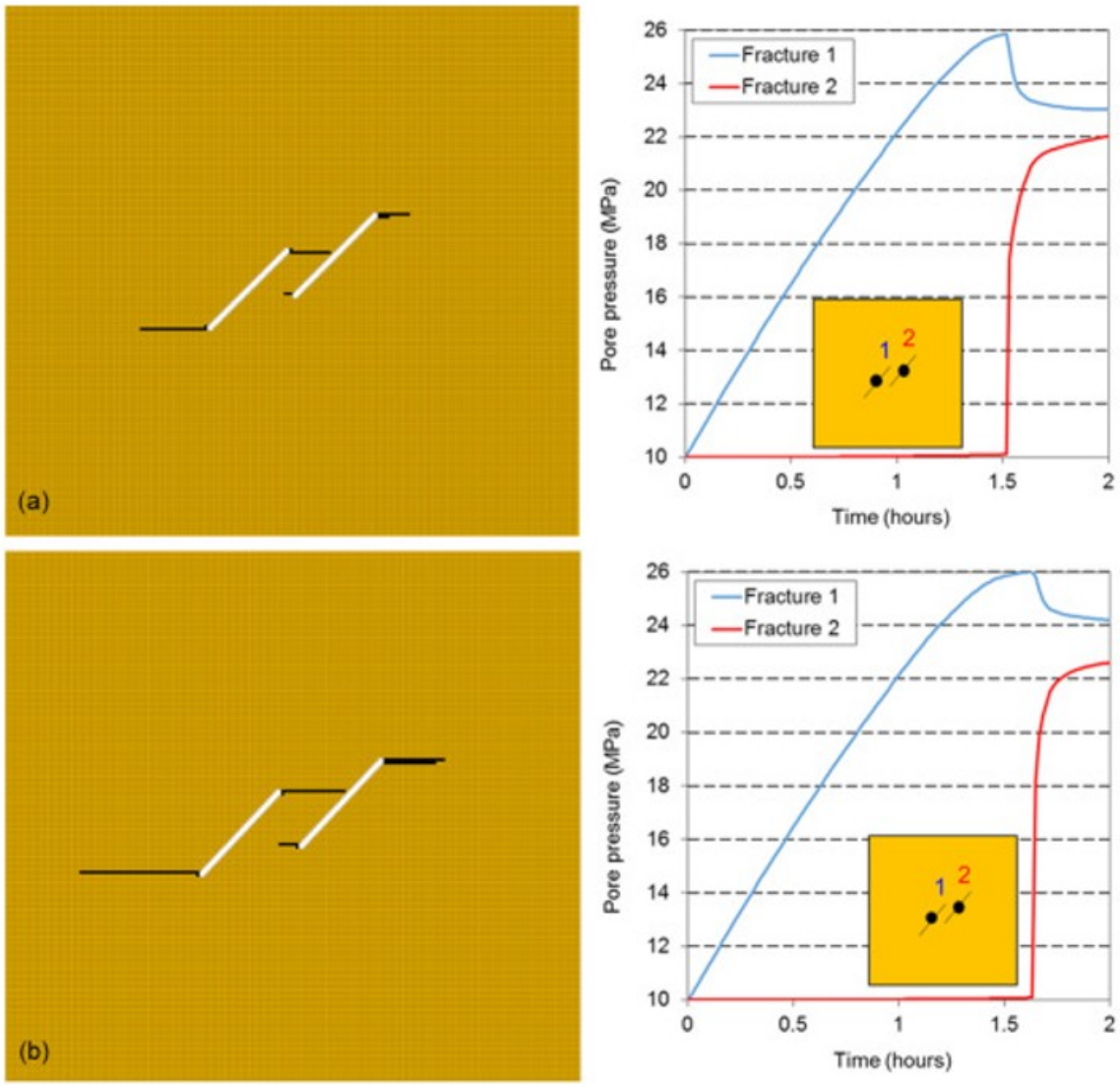

Fig. 12. Tension failure regions (left) and variation with time (hours) of fluid pore pressure (MPa) (right) obtained with *d* equal to (a) 0.50 m and (b) 0.75 m (results obtained at 2 h of injection for rock domain FD2 with fracture angles $\alpha_1 = \alpha_2 = 45°$).

6.2. Effect of the ratio *SR* between the magnitudes of maximum and minimum horizontal stresses

Fig. 13 shows fracture extensions and fluid pore pressure fields obtained for *SR* equal to 1 and 3. Fig. 14 shows the variation with time of the fluid pore pressure in the centre of the fractures. The results obtained for *SR* equal to 1 show that the fractures do not propagate, and hence, there is no interaction between the two fractures. Consequently, because the intact rock is less permeable than the fractures, the increase in fluid pore pressure in fracture 2 is negligible (less than 0.1 MPa). In fracture 1, the fluid pore pressure increases almost linearly with time during the injection period (Fig. 14). At 2 h of injection, the fluid pore pressure is approximately 32 MPa. A comparison

with the results presented for *SR* equal 2 enables us to conclude that the minimum fluid pore pressure necessary to extend the fractures increases when the boundary stresses have equal magnitude. In this case, to observe fracture propagation, the injection period must be greater than 2 h.

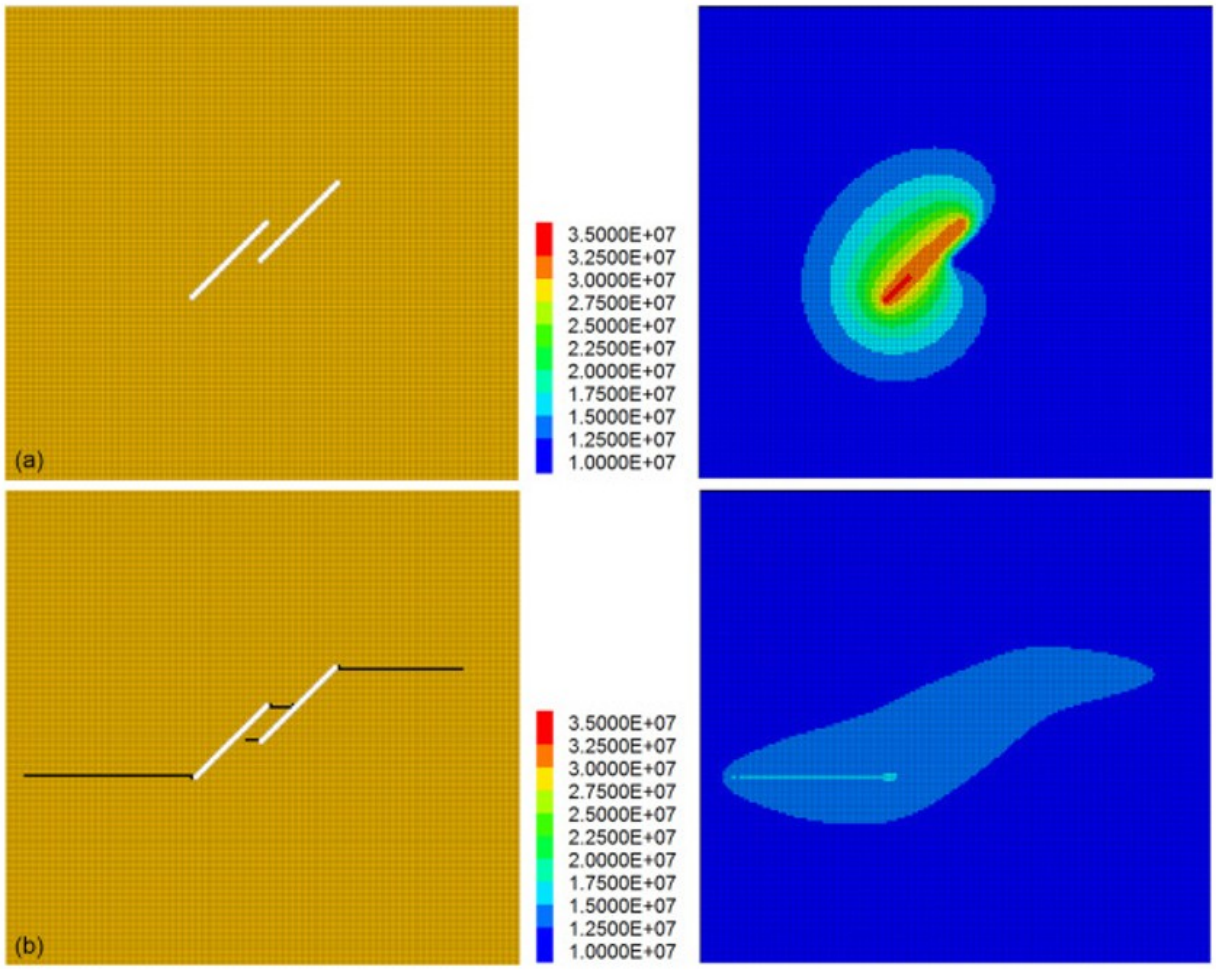

Fig. 13. Tension failure regions (left) and fluid pore pressure fields (Pa) (right) obtained with a stress ratio *SR* equal to (a) 1 and (b) 3 (results obtained at 2 h of injection for rock domain FD2 with fracture angles $\alpha_1 = \alpha_2 = 45°$).

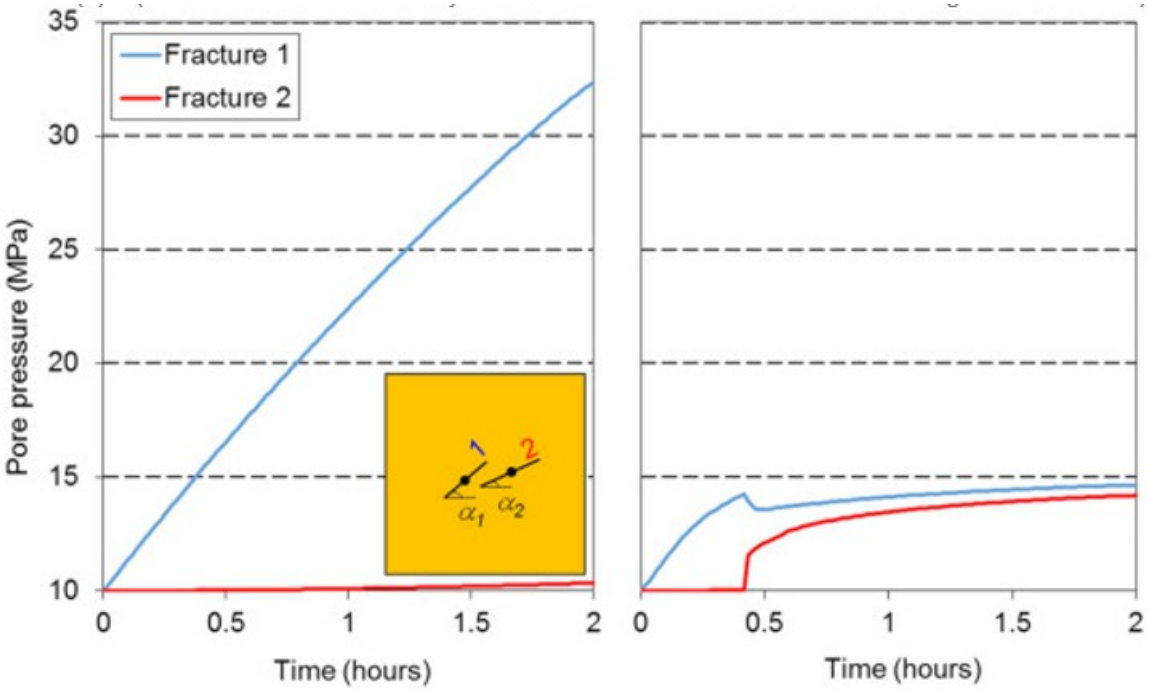

Fig. 14. Variation with time (hours) of the fluid pore pressure (MPa) in the centre of the fractures for fracture rock domain FD2 by considering a stress ratio *SR* of (left) 1 and (right) 3 (results obtained at 2 h of injection for rock domain FD2 with fracture angles $\alpha_1 = \alpha_2 = 45°$).

When *SR* is equal to 3, the fractures propagate approximately 25 cm even before hydraulic fracturing stimulation starts. This immediate fracture extension results from stresses applied at the boundaries and an initial fluid pore pressure of 10 MPa. As a result, the rate of increase in fluid pore pressure with time is slower than those observed for *SR* equal to 1 and 2. In addition, because the principal stress magnitudes around the fractures tips decrease more for larger differential boundary stresses, the fractures connect for a pore pressure significantly smaller (14.2 MPa) than the pressure of 25.5 MPa necessary for fractures to connect when *SR* is equal to 2 (Fig. 8). After the fractures connect, the curves of the variation of fluid pore pressure with time are similar to those obtained for *SR* equal to 2. At 2 h of injection, the fluid pore pressures in fractures 1 and 2 are approximately 14.6 and 14.2 MPa, respectively, and the extension of fracture 1 is approximately 3.10 m, which is 2.75 m more than that obtained for a stress ratio of 2 (Fig. 5, Fig. 7). These calculations illustrate the important role of the maximum principal stress magnitude on the propagation of existing fractures when they are stimulated by hydraulic fracturing.

6.3. Effect of the permeability k_R of the intact rock

In this section, the influence of the permeability k_R of the intact rock on the simulation results is analysed by considering two additional values for k_R: 10^{-17} and 10^{-16} m^2. The results for tension failure regions and fluid pore pressure fields are presented in Fig. 15, and they are compared with those obtained for k_R equal to 10^{-18} m^2. These results show that when $k_R$increases by one

order of magnitude, the fracture propagation decreases by 15 cm. When k_R increases by two orders of magnitude, no fracture propagation is observed. The pore pressure in fracture 1 decreases approximately 1 and 4.5 MPa when k_R increases by one and two orders of magnitude, respectively. This analysis shows that, as k_R increases, the fracture propagation decreases because of the dissipation of pressure into the rock matrix and the resulting decrease in the pressure build-up around the fracture tips.

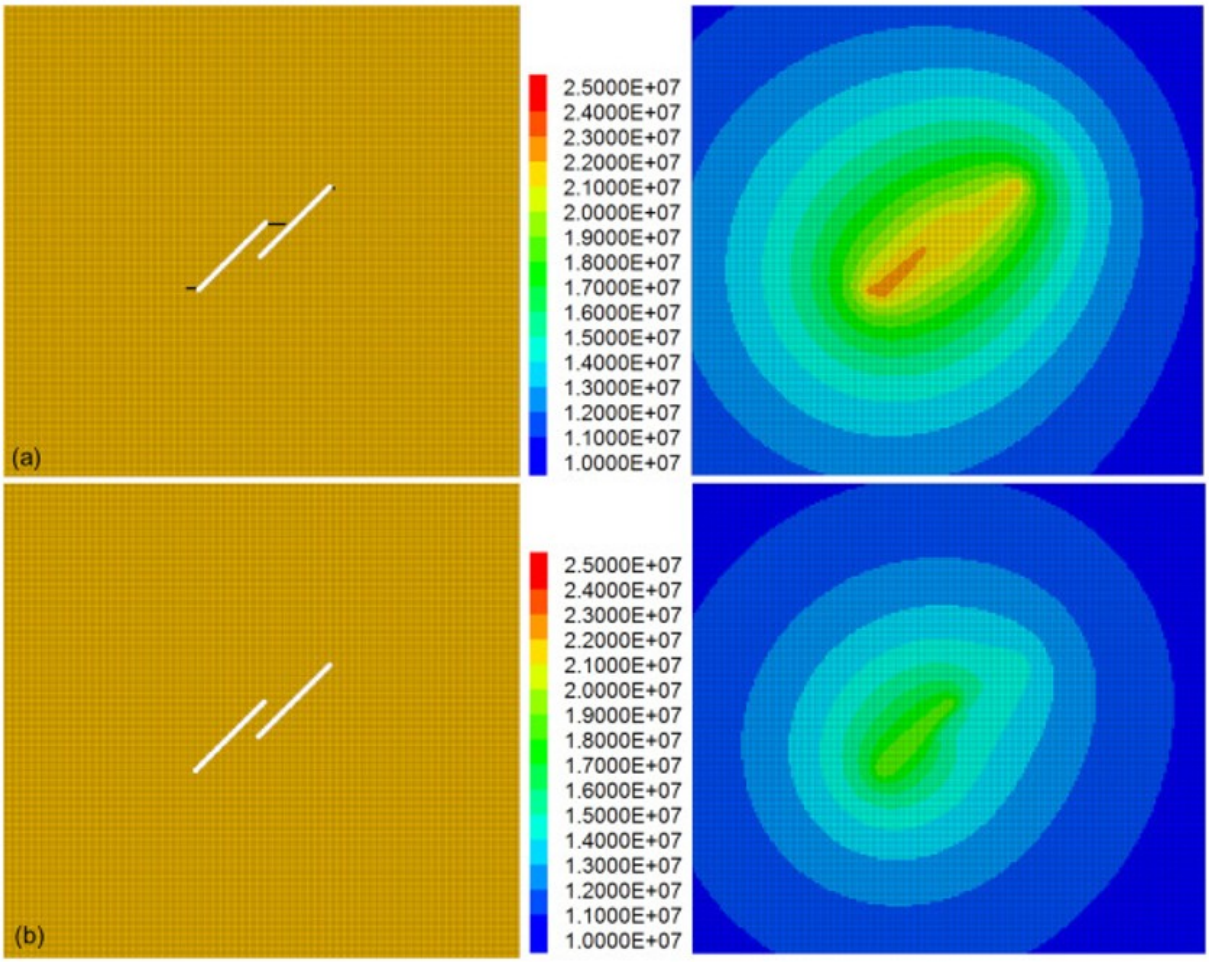

Fig. 15. Tension failure regions (left) and fluid pore pressure fields (Pa) (right) obtained with a permeability k_R of the intact rock equal to (a) 10^{-17} m^2 (b) 10^{-16} m^2 (results obtained at 2 h of injection for rock domain FD2 with fracture angles $\alpha_1 = \alpha_2 = 45°$).

6.4. Effect of the initial permeability k_{TF} of the tension failure regions

Fig. 16 shows the fracture extensions and fluid pore pressure fields obtained for an initial permeability k_{TF} of the failure regions equal to 4.5×10^{-15} m^2, 4.5×10^{-16} m^2 and 4.5×10^{-18} m^2. The results show that when k_{TF} decreases by one order of magnitude from 4.5×10^{-14} m^2 to 4.5×10^{-15} m^2, the extensions of fractures 1 and 2 decrease by approximately 10 and 25 cm, respectively. The difference between the maximum values in fluid pore pressure observed at the centre of the two fractures increases from 0.6 to 2.1 MPa. This effect occurs because as k_{TF} decreases, it is more difficult for

fluid to penetrate into the recently created fracture, and hence, the fluid pore pressure increases more in the fracture where hydraulic fracturing occurs. When k_{TF} decreases by two orders of magnitude, this difference in fluid pore pressure in the two fractures increases to 4.7 MPa, and the propagation of fracture 2 is only 10 cm. In contrast, fracture 1 propagation increases by 0.35 m. When k_{TF} is set to 4.5×10^{-18} m^2, fracture 1 propagates 20 cm more than in the case of k_{TF} equal to 4.5×10^{-16} m^2, but fracture 2 does not propagate. Because of the changes in volumetric strains, the permeability of the tension failure elements increases by two orders of magnitude with respect to their initial permeability k_{TF}. These values are not enough to lead to significant flow in fracture 2, and the difference in fluid pore pressure between fractures 1 and 2 increases to 20 MPa. In this case, there is practically no pore pressure build-up in fracture 2. This conclusion implies that the results are more sensitive to the initial permeability k_{TF} of the failure regions than to changes in volumetric strains in the elements subjected to tension failure.

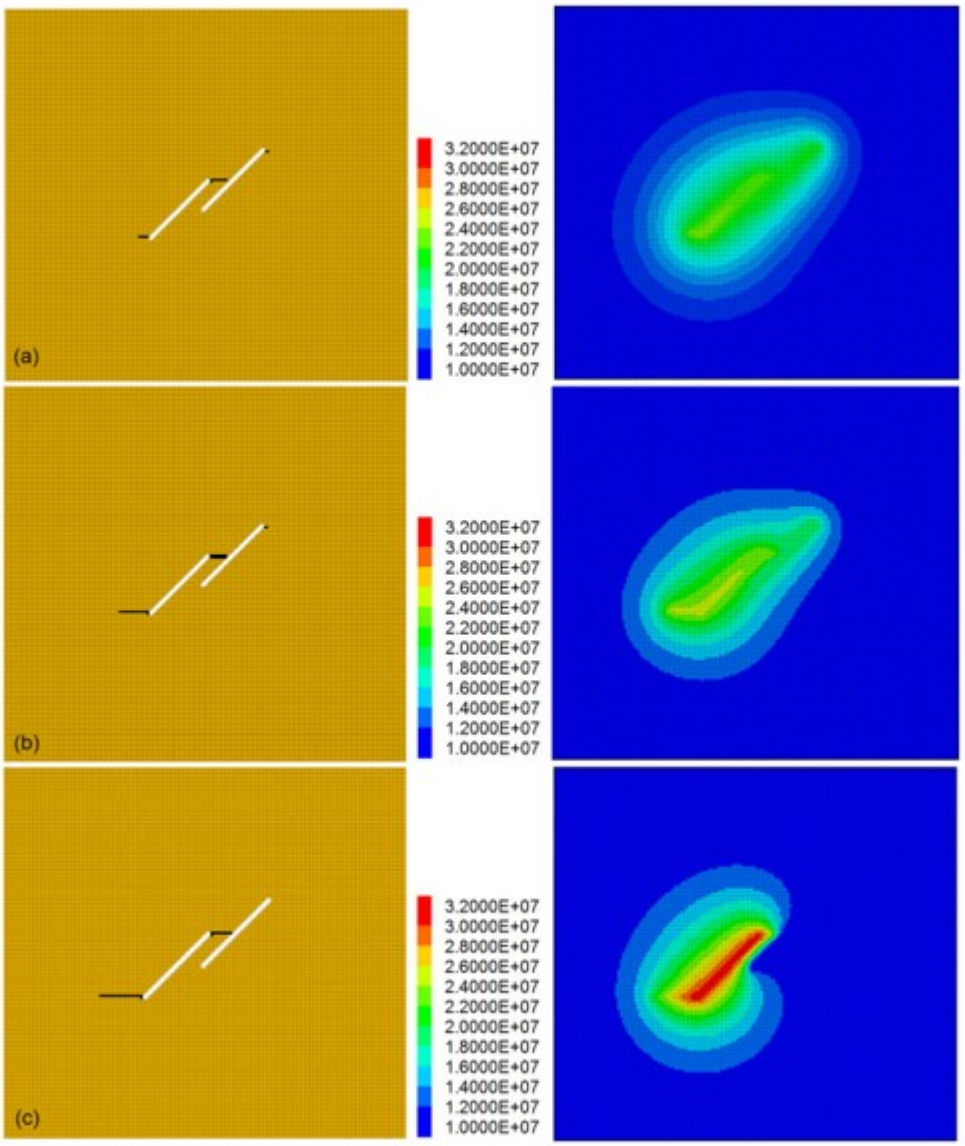

Fig. 16. Tension failure regions (left) and fluid pore pressure fields (Pa) (right) obtained with a permeability k_{TF} of the tension failure regions equal to (a) 4.5×10^{-15} m^2 (b) 4.5×10^{-16} m^2 and (c) 4.5×10^{-18} m^2(results obtained at 2 h of injection for rock domain FD2 with fracture angles $\alpha_1 = \alpha_2 = 45°$).

7. Concluding remarks

The focus of the present study is on the influence of a neighbouring fracture on a fracture subjected to increased fluid pressure during hydraulic fracturing stimulation. This study is accomplished by a comparative coupled hydro-mechanical analysis of two rock domains: FD1, with one natural fracture, and FD2, with two adjacent parallel or non-parallel natural fractures. Hydraulic fracturing is assumed to occur by high-pressure injection into the single fracture in FD1 and one of the two fractures in FD2. Simulations are made for a time period of 3 h with an injection period of 2 h. A base case is considered in which the closest distance d_F between the two natural fractures is 0.25 m, the ratio SR between the magnitude of the

maximum and minimum boundary stresses is set at 2, the permeability k_R of the intact rock is set at 10^{-18} m^2 and the initial permeability k_{TF} of the tension failure regions is considered equal to the initial permeability of the natural fractures. The conclusions from the obtained results may be summarised as follows:

First, the minimum fluid pore pressure necessary to initiate fracture propagation is smaller than the minimum boundary stress magnitude (approximately 85%). This result occurs because the natural fractures have softer properties than the intact rock, and the minimum principal stress at the tips is smaller than the minimum boundary stress magnitude. The fractures start to propagate when the local tensile stress around the tip of the fracture, induced by an increase in pore pressure, is larger than the tensile strength of the intact rock. It is found that, until the fractures start to propagate, the pore pressure in the pressurised fracture increases with time, but this relation is not perfectly linear because of fluid pore pressure diffusion into the permeable intact rock. In contrast, with the FD1 case, in the case of FD2, the pressure in the pressurised fracture decreases significantly (approximately 15%) after it connects with the second fracture.

Second, in a double fracture case with parallel fractures, the results obtained with angles between the two fractures and the maximum principal stress direction (horizontal) of 30° and 45° are found to be similar. However, when the fractures are inclined at an angle of 60°, they are sub-perpendicular to the maximum principal stress direction, and hence, the propagation of fractures is smaller. The fractures connect after an injection period larger than that observed for an angle equal to 30° or 45°, and as a result, in the former case, the fluid pore pressure increases more in the fracture subjected to water injection. When the fractures are non-parallel, it is found that, as the angle between the non-pressurised fracture and the maximum boundary stress direction increases, the time necessary for fractures to connect decreases, the increase in pore pressure is less, and hence, the fracture propagation decreases.

Third, the propagation of a single fracture caused by water injection is larger than that obtained with the presence of a neighbouring second fracture. This effect occurs because in the latter case, the pore pressure decreases when the two fractures connect, and becomes smaller than the minimum pressure necessary to continue propagating the fracture.

Fourth, in a single fracture case, changes in fracture permeability are found to be larger than those obtained in a double fracture case. This difference develops because in the latter case, the pore pressure in the pressurised fracture decreases when the fractures connect, and thus, changes in the fracture apertures are smaller than in the former case. However, changes in fracture permeability are not very significant. At 2 h of injection, the maximum ratio between the final and initial fracture permeability is

approximately 3. Consequently, after the fractures start to propagate, the pore pressure in the pressurised fracture is still increasing.

A sensitivity study is conducted to analyse the influence of the key parameters noted above on the obtained results for the particular case of FD2 with parallel fractures inclined at an angle of 45°. It is found that:

1. When the distance d_F between the two natural fractures increases, the pressurised fracture extends more, and the effect of linkage between fractures on their propagation decreases. At the limit, for a very large d value, the results obtained for the single and double fracture cases are expected to be very similar.

2. When the ratio SR between the boundary stress magnitudes increases, the minimum fluid pore pressure value necessary to initiate fracture propagation decreases. This change occurs because when SR increases, the minimum principal stress around the fracture tip decreases.

3. When the permeability k_R of the intact rock increases, the pore pressure around the fracture tip decreases, which results in a decrease in the fracture propagation. On the other hand, it is found that when the permeability k_{TF} decreases, the fractures may connect, but the difference in fluid pore pressure observed in the two fractures increases. This effect occurs because when the tension failure regions are more impermeable, the flow between the two fractures is less. This relationship illustrates that differences in results are more sensitive to the initial permeability of the tension failure regions than to stress-induced changes in their apertures.

To summarise, fracture propagation is found to be more sensitive to d and SR than to the other parameters. The conclusions from the present study emphasise several interesting aspects of fracture rock hydro-mechanics that deserve further studies, and these effects should be accounted for in modelling hydro-mechanical behaviour of fractured rocks during a hydraulic fracturing operation. As further work, we plan to extend the methodology presented in this paper to study fracture propagation both in three-dimensional space and explore effects of multiple fractures in a realistic fracture network.

Acknowledgments

The authors gratefully acknowledge the Swedish Geological Survey (SGU), grant number 1724, and the EU project, grant number 640979, for providing financial support to research reported in this paper. Additional support was provided by the U.S. Department of Energyunder contract No. DE-AC02-05CH11231.

References

P. Areias, T. Rabczuk, D. Dias da CostaElement-wise fracture algorithm based in rotation of edges Eng. Fract. Mech., 110 (2013), pp. 113-137

P. Areias, M. Msekh, T. RabczukDamage and fracture algorithm using the screened Poisson equation and local remeshing Eng. Fract. Mech., 158 (2016), pp. 116-143

P.B. Attewell, I.W. FarmerPrinciples of Engineering Geology John Wiley & Sons Inc., New York (1976)

A. Bobet, H.H. EinsteinFracture coalescence in rock-type materials under uniaxial and biaxial compression Int. J. Rock Mech. Min. Sci., 35 (7) (1998), pp. 863-888

F. Cappa, J. RutqvistModeling of coupled deformation and permeability evolution during fault reactivation induced by deep underground injection of CO_2 Int. J. Greenhouse Gas Control, 5 (2011), pp. 336-346

L.Y. Chin, R. Raghavan, L.K. ThomasFully coupled geomechanics and fluid flow analysis of wells with stress-dependent permeability Soc. Petrol. Eng., 5 (2000), pp. 32-45

Z. Fang, J.P. HarrisonDevelopment of a local degradation approach to the modeling of brittle fracture in heterogeneous rocks Int. J. Rock Mech. Min. Sci., 39 (2002), pp. 443-457

Z. Fang, J.P. HarrisonApplication of a local degradation model to the analysis of brittle fracture of laboratory scale rock specimens under triaxial conditions Int. J. Rock Mech. Min. Sci., 39 (2002), pp. 459-476

B. Figueiredo, C.F. Tsang, J. Rutqvist, A. NiemiA study of changes in deep fractured rock permeability due to coupled hydro-mechanical effects Int. J. Rock Mech. Min. Sci., 79 (2015), pp. 70-85

P.P. Fu, S.M.S.M. Johnson, C.R.C.R. CarriganAn explicitly coupled hydro-geomechanical model for simulating hydraulic fracturing in arbitrary discrete fracture networks Int. J. Numer. Anal. Methods Geomech., 37 (14) (2013), pp. 2278-2300

L. Germanovich, D. AskakhovFracture closure in extension and mechanical interaction of parallel joints J. Geophys. Res., 109 (2004), p. B02208, 10.1029/2002JB002131

B. Gonçalves da Silva, H.H. EinsteinModeling of crack initiation, propagation and coalescence in rocks Int. J. Fract., 182 (2) (2013), pp. 167-186

Itasca, FLAC3DVersion 5.0. User's Manual Itasca Consulting Group, Minneapolis (2012)

L.J. Ji, A. Settari, R. SullivanA novel hydraulic fracturing model fully coupled with geomechanics and reservoir stimulation Soc. Pet. Eng. J., 14 (3) (2009), pp. 423-430

B. LecampionAn extended finite element method for hydraulic fracture problems

Commun. Numer. Methods Eng., 25 (2009), pp. 121-133

Y. Li, H. Zhou, W. Zhu, S. Li, J. LiuNumerical study of crack propagation in brittle joined rock mass influenced by fracture water pressure Materials, 8 (2015), pp. 3364-3376

A. Manouchehrian, M. Sharifzadeh, M.F. Marji, J. GholamnejadA bonded particle model for analysis of the flaw orientation effect on crack propagation mechanism in brittle materials under compression Arch. Civ. Mech. Eng., 14 (2014), pp. 40-52

S.I. Mayer, S. Stanchits, C. Langenbruch, G. Dresen, S. ShapiroAcoustic emission induced by pore-pressure changes in sandstone samples Geophysics, 76 (3) (2011), pp. MA21-MA32

K.B. Min, J. Rutqvist, C.F. Tsang, L. JingStress-dependent permeability of fractured rock masses: a numerical study Int. J. Rock Mech. Min. Sci., 41 (2004), pp. 1191-1210

N. Moes, T. BelytschkoA finite element method for growth without remeshing Int. J. Numer. Methods Eng., 46 (1) (1999), pp. 131-150

T.T. Mohammadnejad, A.A. KhoeiAn extended finite element method for hydraulic fracture propagation in deformable porous media with the cohesive crack model Finite Elem. Anal. Des., 73 (0) (2013), pp. 77-95

S. Morgan, C. Johnson, H. EinsteinCracking processes in Barre granite: fracture process zones and crack coalescence Int. J. Fract., 180 (2013), pp. 177-204

O. Mutlu, D. PollardOn the patterns of wing crack along an outcrop scale flaw: a numerical modeling approach using complementarity J. Geophys. Res., 113 (2008), p. B06403, 10.1029/2007JB005284

V.P. Nguyen, H. Lian, T. Rabczuk, S. BordasModelling hydraulic fractures in porous media using flow cohesive interface Eng. Geol. (2017), 10.1016/j.enggeo.2017.04.010

S.S. Oterkus, E.E. Madenci, E.E. OterkusFully coupled poroelastic peridynamic formulation for fluid-filled fractures Eng. Geol. (2017), pp. 1-26

C.J. Pearce, A. Thavalingam, Z. Liao, N. BićanićComputational aspects of the discontinuous deformation analysis framework for modelling concrete fracture Eng. Fract. Mech., 65 (2000), pp. 283-298

D.D. Pollard, P. SegallTheoretical displacements and stresses near fractures in rock: with applications to faults, joints, veins, dikes, and solution surfaces B.K. Atkinson (Ed.), Fracture Mechanics of Rock, Academic Press Inc (1987), pp. 277-349

D.O. Potyondy, P.A. CundallA bonded-particle model for rock Int. J. Rock Mech. Min. Sci., 41 (2004), pp. 1329-1364

K. Pruess, C. Oldenburg, G. MoridisTOUGH2 user's guide, version 2.0 Lawrence Berkeley National Laboratory Report LBNL-43134, Lawrence Berkeley National Laboratory, Berkeley, California (2011), p. 198

T. Rabczuk, G. Zi, S. Bordas, H. Nguyen-XuanA simple and robust three-dimensional cracking-particle method without enrichment Comput. Methods Appl. Mech. Eng., 199 (2010), pp. 2437-2455

A. Rinaldi, J. Rutqvist, F. CappaGeomechanical effects of CO_2 leakage through fault zones during large-scale underground injection Int. J. Greenhouse Gas Control, 20 (2014), pp. 117-131

J. Rutqvist, O. StephanssonThe role of hydro-mechanical coupling in fractured rock engineering Hydrogeol. J., 11 (2013), pp. 7-40

J. Rutqvist, A. Bäckström, M. Chijimatsu, X.-T. Feng, P.-Z. Pan, J. Hudson, L. Jing, A.Kobayashi, T. Koyama, H.-S. Lee, X.-H. Huang, M. Rinne, B. ShenMultiple-code simulation study of the long-term EDZ evolution of geological nuclear waste repositories Environ. Geol., 57 (2009), pp. 1313-1324

J. Rutqvist, C. Leung, A. Hoch, Y. Wang, Z. WangLinked multicontinuum and crack tensor approach for modeling of coupled geomechanics, fluid flow and transport in fractured rock J. Rock Mech. Geotech. Eng., 5 (2013), pp. 18-31

C.F. Tsang, A. NiemiDeep hydrogeology: a discussion of issues and research needs Hydrogeol. J., 21 (2013), pp. 1687-1690

B. Vásárhelyi, A. BobetModelling of crack initiation, propagation and coalescence in uniaxial compression Rock Mech. Rock. Eng., 33 (2) (2000), pp. 119-139

P.A. Witherspoon, J.S.Y. Wang, K. Iwai, J.E. GaleValidity of cubic law for fluid flow in a deformable rock fracture Water Resour. Res., 16 (1980), pp. 1016-1024

L.N.Y. Wong, H.H. EinsteinCrack coalescence in molded gypsum and Carrara marble: part 1 – macroscopic observations and interpretation Rock Mech. Rock. Eng., 42 (3) (2009), pp. 475-511

L.N.Y. Wong, H.H. EinsteinCrack coalescence in molded gypsum and Carrara marble: part 2 – macroscopic observations and interpretation Rock Mech. Rock. Eng., 42 (3) (2009), pp. 513-545

S.Q. Yang, Y.H. Huang, H.W. Jing, X.R. LiuDiscrete element modeling on fracture coalescence behavior of red sandstone containing two unparallel fissures under uniaxial compression Eng. Geol., 178 (2014), pp. 28-48

A. Zang, C. Wagner, S. Stanchits, G. Dresen, R. Andresen, M. HaidekkerSource analysis of acoustic emissions in Aue granite cores under

symmetric and asymmetric compressive loads Geophys. J. Int., 135 (1998), pp. 1113-1130

Zhang X and Sanderson D. Evaluation of instability in fractured rock masses using numerical analysis methods: effects of fracture geometry and loading direction. J. Geophys. Res. 106 (B11): 26671–687.

J. Zhao (Ed.), Rock Mechanics for Civil Engineering (2008)

(49 pp.) www.epf.ch/en/ensei/Rock-Mechanics/ENS-080312-EN-Notes-Chapter-4.pdf

X. Zhuang, R. Huang, C. Liang, T. RabczukA coupled thermo-hydro-mechanical model of jointed hard rock for compressed air energy storage Math. Probl. Eng. (2014), p. ID179169, 10.1155/2014/179169

X. Zhuang, Q. Wang, H. ZhuMultiscale modelling of hydro-mechanical couplings in quasi-brittle materials Int. J. Fract., 204 (2017), pp. 1-27